

Controlled delivery of a neurotransmitter-agonist conjugate for functional recovery after severe spinal cord injury

Received: 15 February 2022

Accepted: 4 May 2023

Published online: 12 June 2023

Yanming Zuo^{1,2,3,7}, Jingjia Ye^{1,2,3,7}, Wanxiong Cai^{2,3}, Binjie Guo^{2,3}, Xiangfeng Chen^{2,3}, Lingmin Lin^{1,2,3}, Shuang Jin^{2,3}, Hanyu Zheng^{2,3}, Ao Fang^{2,3}, Xingran Qian^{2,3}, Zeinab Abdelrahman^{1,2,3}, Zhiping Wang^{1,2,3}, Zhipeng Zhang^{1,2,3}, Zuobin Chen¹, Bin Yu⁵, Xiaosong Gu⁵ & Xuhua Wang^{1,2,3,6}  

 Check for updates

Despite considerable unmet medical needs, effective pharmacological treatments that promote functional recovery after spinal cord injury remain limited. Although multiple pathological events are implicated in spinal cord injuries, the development of a microinvasive pharmacological approach that simultaneously targets the different mechanisms involved in spinal cord injury remains a formidable challenge. Here we report the development of a microinvasive nanodrug delivery system that consists of amphiphilic copolymers responsive to reactive oxygen species and an encapsulated neurotransmitter-conjugated KCC2 agonist. Upon intravenous administration, the nanodrugs enter the injured spinal cord due to a disruption in the blood–spinal cord barrier and disassembly due to damage-triggered reactive oxygen species. The nanodrugs exhibit dual functions in the injured spinal cord: scavenging accumulated reactive oxygen species in the lesion, thereby protecting spared tissues, and facilitating the integration of spared circuits into the host spinal cord through targeted modulation of inhibitory neurons. This microinvasive treatment leads to notable functional recovery in rats with contusive spinal cord injury.

Most cases of spinal cord injury (SCI) in humans are anatomically incomplete, meaning that some connections in the neuronal circuits near, above and below the lesion are spared. However, at least two major pathological processes prevent these spared connections from functioning. First, cell death and blood vessel disruption resulting from traumatic injury trigger inflammation and the production of cytotoxic

factors such as reactive oxygen species (ROS) through a process termed secondary injury, further damaging the spinal connections that were spared in the primary injury and exacerbating functional deficits^{1,2}. Intensive efforts have been made in the past decade to develop protective treatment strategies that can rescue spared spinal connections, such as the transplantation of neuroprotective materials^{3–5}.

¹Department of Neurobiology and Department of Rehabilitation Medicine, First Affiliated Hospital, Zhejiang University School of Medicine, Hangzhou, P. R. China. ²Liangzhu Laboratory, MOE Frontier Science Center for Brain Science and Brain-machine Integration, State Key Laboratory of Brain-machine Intelligence, Zhejiang University, Hangzhou, China. ³NHC and CAMS Key Laboratory of Medical Neurobiology, Zhejiang University, Hangzhou, China.

⁴School of Chemistry and Molecular Engineering, Frontiers Science Center for Materiobiology and Dynamic Chemistry, East China University of Science & Technology, Shanghai, P. R. China. ⁵Key Laboratory of Neuroregeneration of Jiangsu and Ministry of Education, Nantong University, Nantong, P. R. China.

⁶Co-innovation Center of Neuroregeneration, Nantong University, Nantong, P. R. China. ⁷These authors contributed equally: Yanming Zuo, Jingjia Ye.

 e-mail: xhw@zju.edu.cn

However, these procedures might further damage the injured spinal cord and result in unpredictable side effects. Second, SCI triggers massive alterations in excitability, disrupting the overall balance of neural circuits in the injured spinal cord^{6–8}. Previous studies have reported that inhibition of inhibitory, but not excitatory, interneurons via genetic activation of KCC2 can increase overall excitability and transform initially dormant relay or endogenous spinal cord circuits into a functional state after SCI^{6,9}. However, whether this strategy is efficacious in clinically translatable SCI models is not yet clear. In addition, the development of a microinvasive pharmacological approach to selectively target inhibitory neurons and alter their activity remains the bottleneck for the clinical application of this strategy¹⁰.

Disguising drugs as neurotransmitters can promote their delivery into neurons that synthesize these neurotransmitters^{11–13}. Thus, we hypothesized that a similar strategy could be used to deliver drugs that target inhibitory interneurons. Specifically, we conjugated the drug (Z)-5-(4-fluoro-2-hydroxybenzylidene)-2-(tetrahydropyridazin-1(2H)-yl)thiazol-4(5H)-one (CLP-257), a verified KCC2 activator that reduces intracellular chloride concentrations and decreases neuronal excitability^{14–16}, to γ-aminobutyric acid (GABA) or dopamine^{17–19}, which have been reported to play important roles in motor control^{11,20–22}. To facilitate microinvasive administration and ROS-responsive release, an amphiphilic block copolymer with a polyethylene glycol (PEG)-based hydrophilic segment and a hydrophobic segment with boron-based ROS scavengers was designed and synthesized to encapsulate hydrophobic prodrugs^{23–26}. These micelle-based nanodrugs could be injected intravenously, and ROS-responsively release prodrugs at injury sites^{25,27,28}. Our pharmacological method elicited substantial functional restoration in rats with SCI, indicating a promising direction for therapeutics targeting SCI and other neurological conditions.

Synthesis and characterization of the designed nanodrugs

To specifically target the neurons of interest, the KCC2 agonist CLP-257 (refs. 6,16) was conjugated to the neurotransmitter GABA or dopamine (Fig. 1a). GABA- or dopamine-conjugated prodrugs release CLP-257 after being hydrolysed under physiological conditions. The structures of these synthesized prodrugs were confirmed by ¹H-NMR (Supplementary Fig. 1). However, the synthesized prodrugs were hydrophobic and had poor solubility in physiological environments, limiting their applicability and efficacy for non-invasive administration. To overcome these limitations, an amphiphilic block copolymer with a PEG-based hydrophilic segment and a hydrophobic segment with boron-based ROS scavengers was designed to encapsulate these prodrugs.

Through optimization, we synthesized polymer nanocarriers of approximately 108 nm in size and encapsulated prodrugs within their core using the nanoprecipitation method²⁹, achieving high encapsulation efficiency and stability (Supplementary Information and Extended Data Fig. 1). Transmission electron microscopy (TEM) images showed that all nanoparticles exhibit a spherical morphology, with an average size of about 90 nm without the hydration layer (Supplementary Fig. 2g,h). The hydrodynamic diameters of the nanodrugs were slightly enlarged due to drug loading (Fig. 1c). The surface potentials of these nanodrugs were then characterized (Fig. 1d), revealing near neutralization^{30,31}.

We next attempted to determine whether the synthesized nanodrugs responded to ROS-enriched environments. To do this, the empty nanocarriers (called ROS Nano) were tested. After exposed H₂O₂ stimulation, the ROS Nano were analysed by TEM and dynamic light scattering. We found that ROS Nano responded quickly to H₂O₂ stimulation and showed noticeable expansion and collapse (Fig. 1e–g), which is consistent with the findings of previous studies^{25,27,28}. Moreover, the release profiles of Nile red stain encapsulated in ROS Nano were positively dependent on the H₂O₂ concentration (Fig. 1h), suggesting that the nanodrugs are highly sensitive to

ROS stimulation. The nanodrugs were engineered to respond to ROS-enriched environments of SCI lesions. Upon testing, they demonstrated both cytocompatibility and potent antioxidative activity, signifying a robust ability to shield cells from ROS damage (Supplementary Information and Supplementary Fig. 2).

Enhanced lesion localization and targeting efficacy

SCIs compromise the integrity of the spinal cord, resulting in the acute breakdown of the blood–spinal cord barrier (BSCB). This, in turn, leads to the accumulation of inflammatory cells at the lesion site, creating an environment with high levels of toxic ROS²⁶. Since the nanodrugs intensively responded to ROS stimulation, we reasoned that they could responsively release their payloads of prodrugs in the ROS-enriched environment of the injured spinal cord (Fig. 2a). To test this hypothesis, we first optimized a severe tenth thoracic vertebra (T10) contusive SCI model, in which the contusion was prolonged to 5 seconds to maintain a consistent injury severity. Following, we replaced CLP-257 with a fluorescence dye, Cy5.5, to investigate the drug release profiles of the nanoparticles with prodrugs GABA and dopamine hydrochloride (DOPA; named GABA Nano and DOPA Nano, respectively). SCI rats were randomly administered 10 mg kg^{−1} Cy5.5-conjugated GABA Nano (GABA Nano@Cy5.5) or DOPA Nano (DOPA Nano@Cy5.5) through an injection in their tail veins 3 h after SCI; this represented the earliest clinically feasible time point for such a treatment. The spinal cords of the rats were collected at 3, 6, 24 and 48 h after nanodrug administration for further analysis (Fig. 2b).

We found that the nanodrugs intensively accumulated around the spinal lesion site 3 h after injection, reached the maximum concentration at approximately 6 h after injection and persisted for 48 h. This indicates that sufficient spinal tissue had accumulated and that the nanodrugs had a long circulation time, which might benefit in vivo targeted delivery (Fig. 2c). Interestingly, fluorescence distribution analysis indicated that the nanodrugs preferentially accumulated in the rostral region adjacent to the lesion, possibly due to the occurrence of spinal vascular occlusion after severe SCI (Fig. 2d)^{32,33}. The tropism of these nanodrugs in this SCI model facilitates the targeting of propriospinal neurons above the lesion with spared descending projections.

To further characterize the tropism of nanodrugs in the injured spinal cord, longitudinal spinal cord sections were immunostained with GABAergic and dopaminergic neuron markers and subjected to colocalization analysis. We found that several cells labelled with GABA Nano were colocalized with cells that were stained with GABAergic markers (Fig. 2f,h). Similarly, numerous cells labelled with DOPA Nano were colocalized with cells stained with dopaminergic markers (Fig. 2g,i). Quantitative analyses of different rats showed that approximately 80% of the cells labelled with GABA Nano or DOPA Nano were their target neurons (Fig. 2j). Results show the nanodrugs exhibit high selectivity and potency with negligible toxicity (Supplementary Fig. 3). They also preferentially target neurons in the injured spinal cord (Supplementary Fig. 4).

Payload delivery coincides with early BSCB restoration

It is known that the BSCB is restored within seven days post SCI⁹, which prevents macromolecular agents from penetrating in the late stage of SCI³⁴. Fortunately, the restored BSCB still allows the penetration of small molecules or specific peptides or proteins³⁵. Because SCI-induced ROS upregulation lasts for months³⁶, we speculated that the designed nanodrugs might release the encapsulated prodrugs in response to ROS, which could in turn penetrate the injured spinal cord (Fig. 3a). To test this hypothesis, in the same SCI model, we intravenously administered 10 mg kg^{−1} nanodrug of ROS Nano@Cy5.5 to different groups of rats, including intact rats and rats at 4, 7 and 14 days after SCI (Fig. 3b). The rats were killed 6 h after nanodrug injection for analysis.

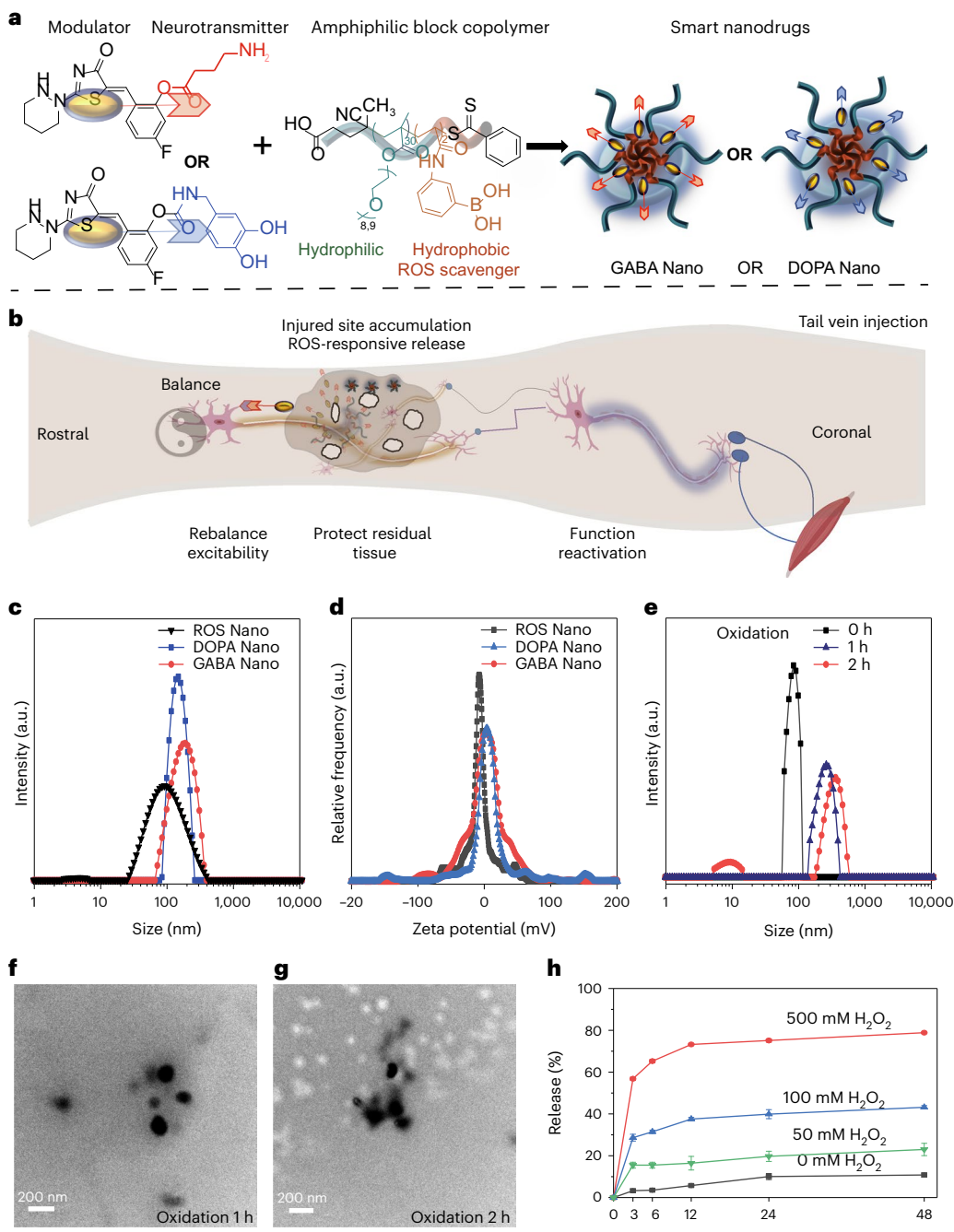


Fig. 1 | Design and characterization of smart nanodrugs. **a**, Schematic depicting the synthesis of smart nanodrugs; nanoparticles share the same amphiphilic polymeric nanocarrier but have different neurotransmitter-functionalized modulators (GABA Nano or DOPA Nano). **b**, Schematic of the mechanisms of the smart nanodrugs after SCI. Following administration by tail vein injection, the smart nanodrugs accumulate in the injury site through ROS-responsive release, consume excess ROS and release neuron-targeted modulators. The effects of nanodrugs include protecting spared tissue/axons, rebalancing the excitability of specific neurons and eventually reactivating the

lumbosacral central pattern generator after SCI. **c,d**, The particle sizes and zeta potentials of empty nanoparticles (ROS Nano), DOPA Nano and GABA Nano.

e, Changes in ROS nanoparticle size after treatment with H_2O_2 (500 mM).

f,g, Representative TEM images of ROS Nano after oxidation by H_2O_2 for 1 h and 2 h. Independent experiments were repeated three times with similar results.

h, The release rates of ROS Nano in the presence of different concentrations of H_2O_2 . Three independent experiments were conducted with similar results. Data are shown as the mean \pm s.e.m.

As a result, we found that the nanodrug could transport Cy5.5 into the spinal cord adjacent to the lesions in rats injected at 4 days or later after SCI (Fig. 3b,c). Surprisingly, the fluorescence intensity was considerably stronger in the rats that were injected 7 days post SCI than in the rats that were injected 4 or 14 days post SCI (Fig. 3b,c), which contradicts our expectation because the BSCB was more resistant to penetration in

the late stage of SCI. A rational explanation for this observation is that drug penetration is not dependent on the penetration of nanoparticles but rather on the disassembly efficiency of nanoparticles. As the ROS level reached its peak at seven days post SCI³⁷, the nanodrugs could disassemble more efficiently and release their small-molecule cargo. Ultimately, more small-molecule compounds penetrated the restored

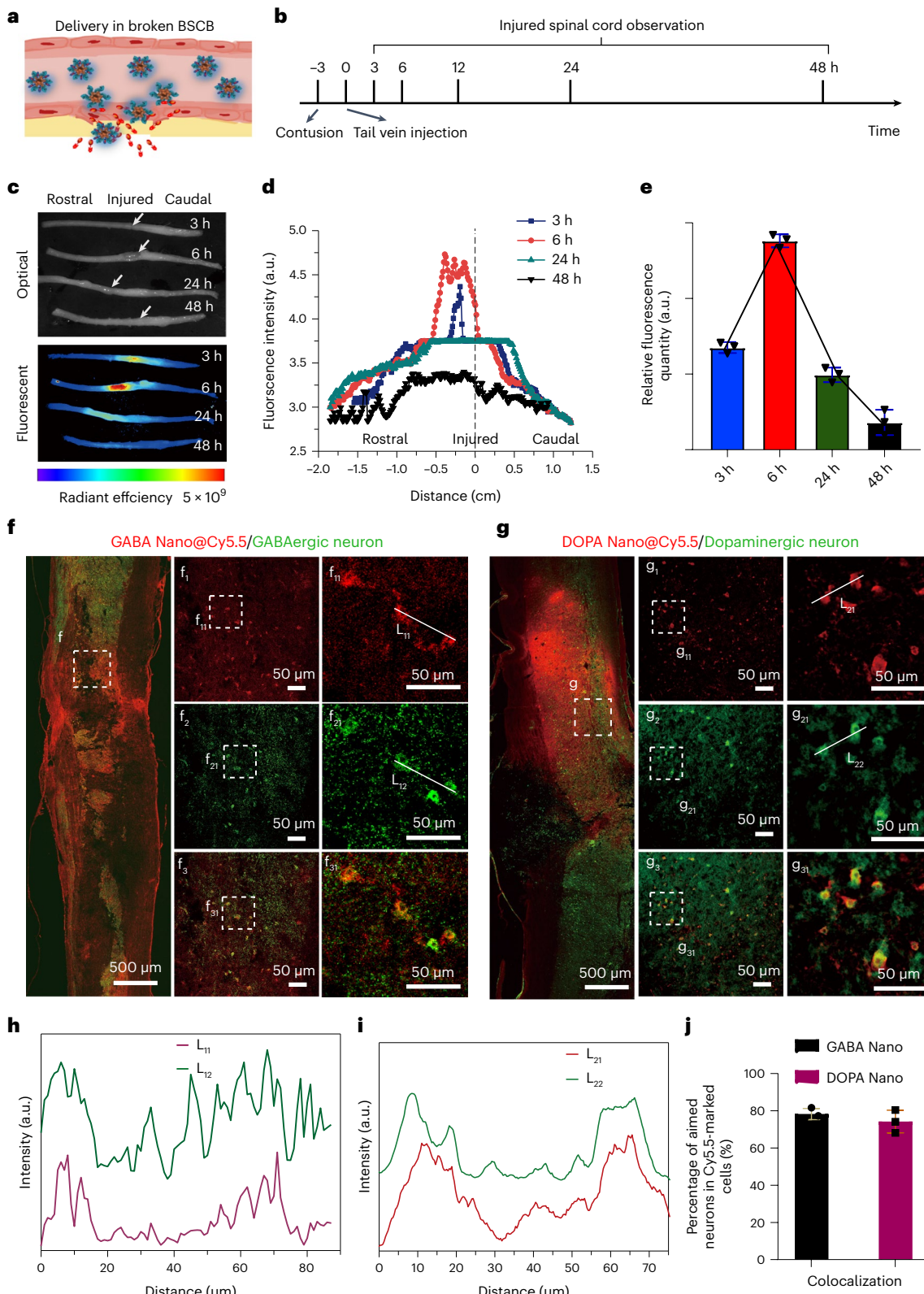


Fig. 2 | Smart nanodrugs accumulate at the injury site in the spinal cord and selectively target specific neurons. **a**, Schematic of nanodrugs reaching and entering the spinal cord following BSCB disruption. **b**, Experimental schedule of SCI, drug delivery and observation. **c**, Images of spinal cords at the indicated time points after SCI and injection of ROS Nano@Cy5.5. The colour bar represents the average radiant efficiency (photons/second/cm²/steradian)/(microwatts/cm²) of in vivo imaging system (IVIS) imaged rats. **d,e**, Spatial and temporal quantification of the fluorescence intensity of ROS Nano@Cy5.5 in the injured spinal cord. $n = 3$ animals for each group. Data are shown as the mean \pm s.e.m.

(red) injection group stained with anti-GABA antibody (green). Regions in the white squares (f, f_1-f_3 and $f_{11}-f_{31}$) are enlarged to the right and show details of cells labelled with GABA Nano and GABAergic neurons near the injury sites. **g**, Representative longitudinal images of tissues from the DOPA Nano@Cy5.5 (red) injection group stained with anti-DOPA antibody (green). Regions in the white squares (g, g_1-g_3 and $g_{11}-g_{31}$) are enlarged to the right. **h,i**, Intensity profiles of the white lines (labelled L) in **f** and **g**. **j**, Quantitative analysis of targeting efficiency via evaluation of the colocalization percentage of target neurons in Cy5.5-marked cells. $n = 3$ animals for each group. Data are shown as the mean \pm s.e.m.

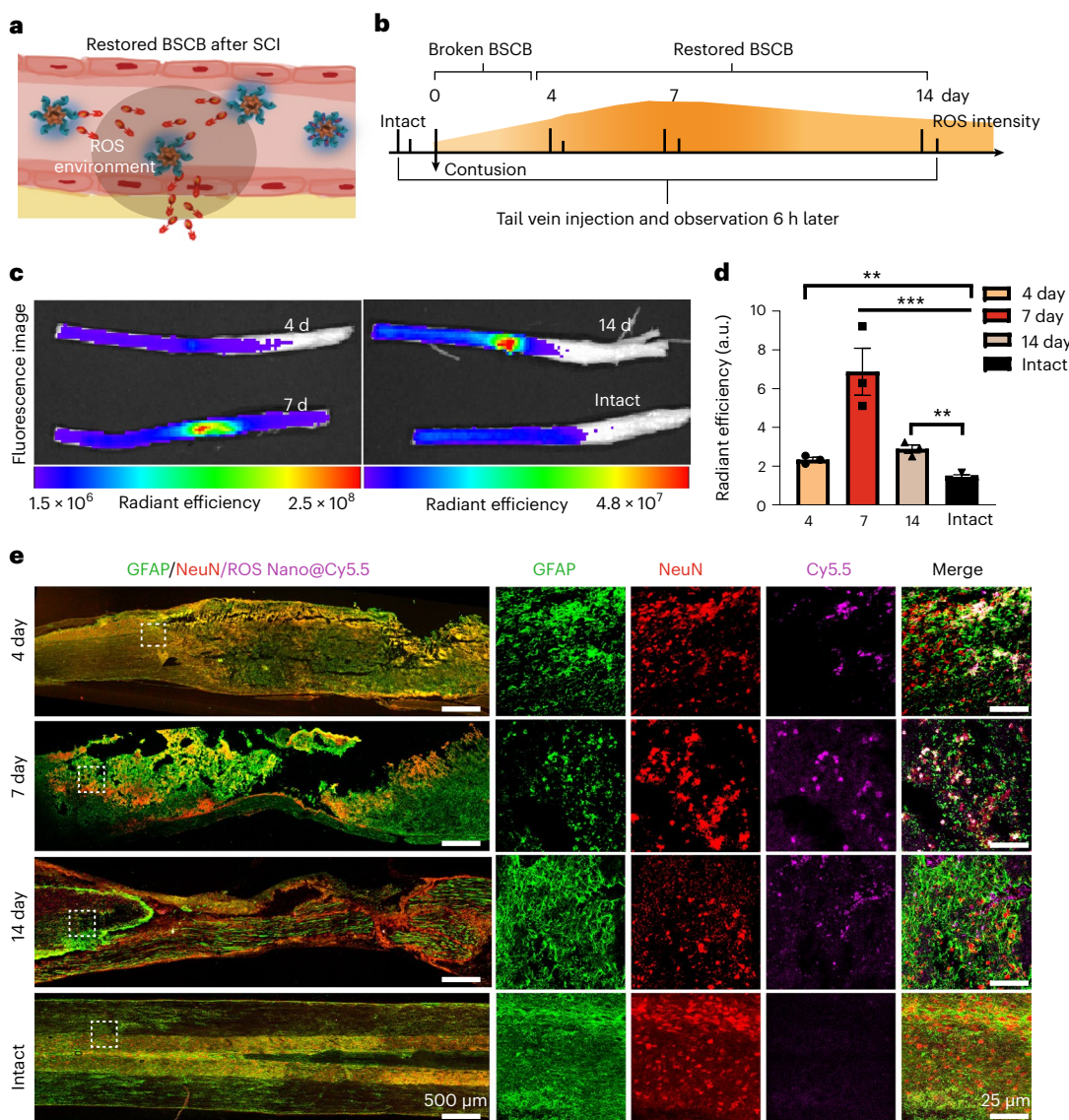


Fig. 3 | The ROS-responsive nanodrug delivery system delivers small molecules into the spinal cord even after BSCB restoration. **a**, Schematic depicting the penetration method of the nanodrug delivery system following restoration of the BSCB. **b**, Schematic diagram of the experimental design. **c**, Representative fluorescent images of spinal cords 6 h after injection. ROS Nano@Cy5.5 was injected at 4, 7 or 14 days post SCI. **d**, Quantitative analysis of spinal cords following ROS Nano@Cy5.5 injection. Data are shown as the mean \pm s.e.m. One-way ANOVA with Tukey's post hoc test was used for

comparisons among multiple groups. $n = 3$ animals for each group. ** $P < 0.01$, *** $P < 0.001$ statistical significance (4-day versus intact, $P = 0.0031$; 7-day versus intact, $P = 0.0003$; 14-day versus intact, $P = 0.0057$). **e**, Representative images of spinal cord sections stained with anti-GFAP antibody (green) and anti-NeuN antibody (red) in ROS Nano@Cy5.5 (magenta)-injected spinal cords. The white dashed boxes indicate the areas shown in the zoomed-in views to the right. $n = 3$ animals for each group. Detailed images and quantification are shown in Supplementary Fig. 4.

BSCB (Fig. 3b,c). Interestingly, we found that approximately 60–70% of Cy5.5-marked cells were neurons, with some variations in different areas of the spinal cord lesion (Supplementary Fig. 5), likely due to the variable microenvironments in and around the lesion. The nanodrugs preferentially targeted neurons instead of astrocytes, possibly because the boron-based parts of the nanocarriers tended to carry their loading close to neurons when the nanocarriers entered the injured spinal cord^{38,39}. However, almost no fluorescence was detected in the spinal cords of intact rats, further confirming that small-molecule penetration in the BSCB was dependent on ROS stimulation (Fig. 3d). To further validate this BSCB penetration method, longitudinal spinal cord sections from these rats were analysed (Fig. 3e). We found that most Cy5.5-marked cells were colocalized with neurons but not glial fibrillary acidic protein (GFAP)-marked astrocytes, suggesting that Cy5.5 penetrated the BSCB and preferentially marked neurons. In addition,

a higher number of Cy5.5-marked cells were observed in the rats that were injected at seven days post SCI, and almost no Cy5.5-marked cells were observed in intact rats, which was consistent with previous observations. Thus, the drug delivery system can deliver hydrophobic small-molecule compounds into the spinal cord even when the BSCB is restored in the late stage of SCI.

Nanodrugs protect spared tissues/axons from secondary injury

After verifying that our nanodrugs were capable of scavenging ROS in vitro and delivering drugs to target neurons, we attempted to assess whether this treatment could ameliorate the SCI-induced neuroinflammatory environment and protect spared tissues/axons from secondary injury. To this end, we employed the same severe T10 contusive SCI model as that used in the drug release study. Unlike the moderate

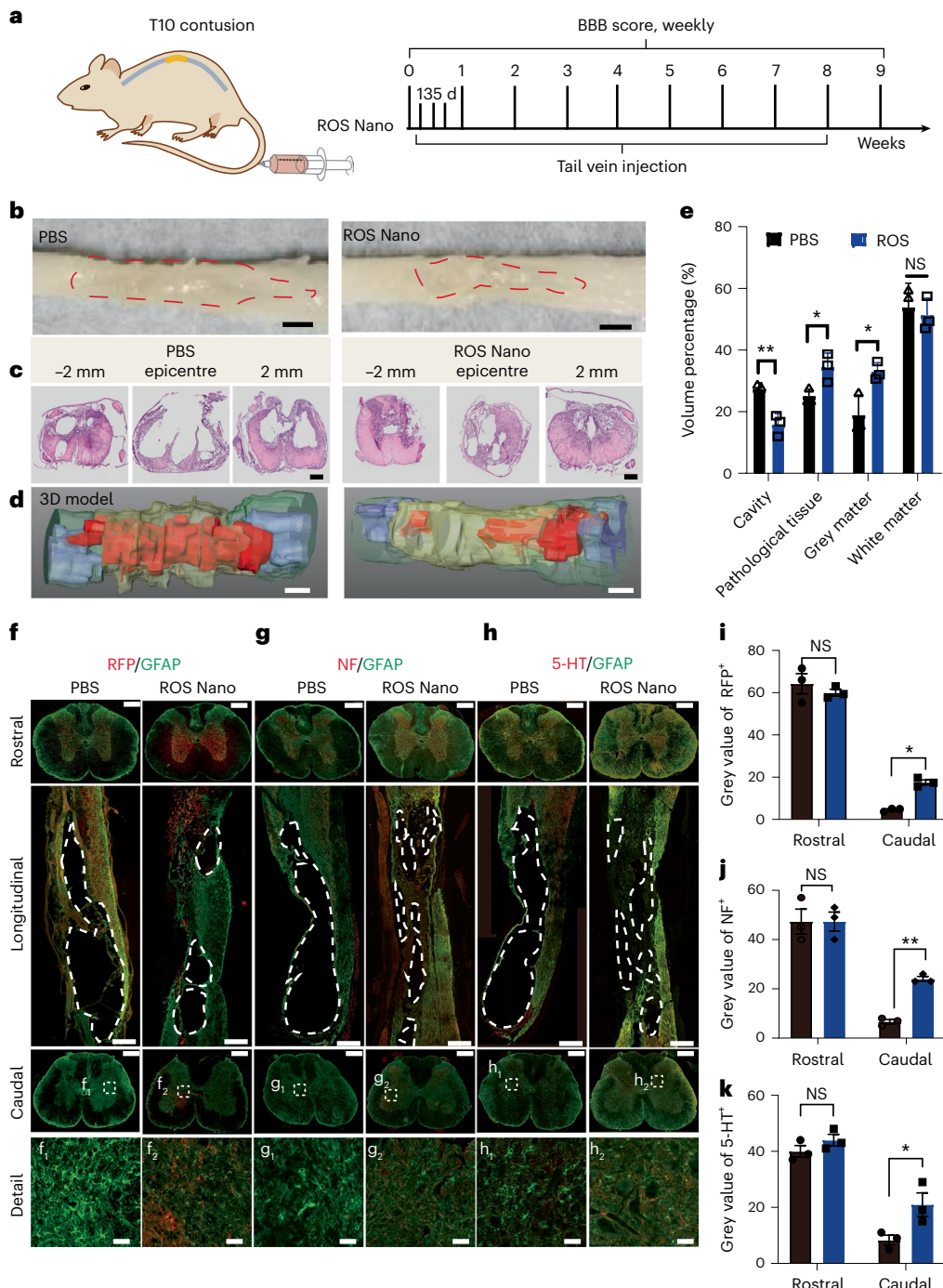


Fig. 4 | ROS Nano treatment protects spared tissues/axons from secondary injury. **a**, Schematic diagram of the experimental design. **b,c**, Representative optical images and H&E-stained images of longitudinal sections of injured spinal cords after nine weeks of treatment. The boundaries of the injury sites are marked with red dashed lines. Spinal cord positions are -2 mm , epicentre and 2 mm relative to the cranial-caudal axis. The epicentre represents the center of injury and serves as the 0 point. Scale bars, 1 cm (**b**) and 1 mm (**c**). $n=3$ animals for each group. **d**, Some 3D reconstruction images of spinal cord tissues showing white matter (green), grey matter (light blue), pathological tissue (yellow) and cavities (red). Scale bars, 1 mm . **e**, Graph showing the quantification of the cavity and pathological volume percentages at the injury site. Data are shown as the mean \pm s.e.m. Two-tailed paired *t*-tests were used for comparisons between two groups (cavity $P=0.007$, pathological $P=0.0343$, white matter $P=0.667$,

black matter $P=0.0260$). $n=3$ rats for each group. * $P<0.05$, ** $P<0.01$; NS, not significant. **f-h**, Representative images of rat spinal cord sections stained with GFAP (green) and NF (red), 5-HT (red) or RFP (red) after nine weeks of treatment with PBS or ROS Nano. The white dashed lines indicate the boundaries of the cavities. Rostral (upper), longitudinal (middle) and caudal (lower) spinal cord sections are shown. The details are shown in the enlarged images of the white dashed boxes (labelled f_1 , f_2 , g_1 , g_2 , h_1 and h_2). $n=3$ animals for each group. Scale bars, $500\text{ }\mu\text{m}$; scale bars for enlarged images, $100\text{ }\mu\text{m}$. **i-k**, Graph showing the quantification of the RFP, NF and 5-HT immunoreactivity grey values on the rostral and caudal sides. Data are shown as the mean \pm s.e.m. Two-tailed paired *t*-tests were used for comparisons between two groups. $n=3$ rats for each group. * $P<0.05$, ** $P<0.01$ (caudal sides RFP, $P=0.0431$; caudal sides NF, $P=0.009$; caudal sides 5-HT, $P=0.0417$).

contusive SCI model with large individual variations, the rats with severe contusive SCI showed minimum ankle movement and exhibited nearly complete hind-limb paralysis within ten weeks after injury. In this study, the examiners were blinded to the drug treatments, and 10 mg kg⁻¹ ROS Nano or phosphate-buffered saline (PBS) was intravenously administered to rats at serial time points after SCI, as detailed in Fig. 4a.

We found that the shape deformation of the spinal cord was obviously less in the rats injected with ROS Nano nine weeks post SCI than in the PBS control group (Fig. 4b), and the hematoxylin and eosin (H&E)-stained images of the spinal cord sections showed that the cystic cavity in the ROS Nano treatment group was notably smaller than that in the PBS-treated rats (Fig. 4c). To quantitatively analyse the cavity volume, images of spinal cross-sections were collected in sequence and reconstructed to three-dimensional (3D) models (Fig. 4d). After quantification across different rats, we found that in the PBS-treated rats, approximately 27.3% of the spinal cord volume was cavities. By contrast, the cavity volume percentage in the rats treated with ROS Nano was significantly decreased to approximately half of that in the PBS-treated rats (-15.8%; Fig. 4e). Compared to the PBS treatment, tissue with an abnormal architecture, which was defined as pathological tissue, was increased in the ROS Nano rats at the injured site (-35% versus 25%). Compared with the rats that received PBS treatment, the rats that received ROS Nano had an increased percentage of grey matter (-33% versus 19%). This may be because the protective effect of ROS Nano reduced cell death, thereby mitigating the formation of cystic cavities and the drastic reduction in grey matter in the epicentre of the lesion⁴⁰. However, there was no difference in the volume proportion of white matter, which may be because of the difference in staining. The white matter was mainly stained by eosin, and the grey matter was stained by hematoxylin. However, the small cystic spaces filled with extracellular matrix-like tissues, which were empty cavities, could be stained by eosin⁴¹.

We next attempted to determine whether more descending axons could survive with this treatment. To this end, the AAV2/9-mCherry were injected into T7–T8 of some rats two weeks before they were killed to trace the descending propriospinal axons, and immunostaining of red fluorescent protein (RFP), anti-neurofilament (NF) and anti-5-hydroxytryptamine (5-HT) was performed to visualize descending propriospinal axons, ubiquitous axonal fibres and serotonergic axons, respectively (Fig. 4f–h). We found that very few axons could extend into the lesion site in all examined subjects. In coronal sections of spinal segments, RFP marked (RFP⁺) propriospinal axons, ubiquitous axonal fibres and serotonergic axons caudal to the lesion were remarkably higher in number in the rats treated with ROS Nano than in the PBS-treated rats (Fig. 4i–k and Extended Data Fig. 2). These results suggested that the axons observed below the lesion sites were spared axons that were recused from secondary injury. Our further research demonstrates that ROS Nano exerts neuroprotective effects

by decreasing neuroinflammation and apoptosis (Supplementary Information, Extended Data Fig. 3 and Supplementary Figs. 5 and 6).

Combining the above neuroprotective results and mechanism analysis, we confirmed that ROS Nano treatment provides a reliable protective effect after SCI. However, the spared tissues preserved by ROS Nano treatment enabled only limited hind-limb locomotor recovery (Supplementary Information and Extended Data Fig. 4).

Treatment improves hind-limb locomotor recovery after SCI

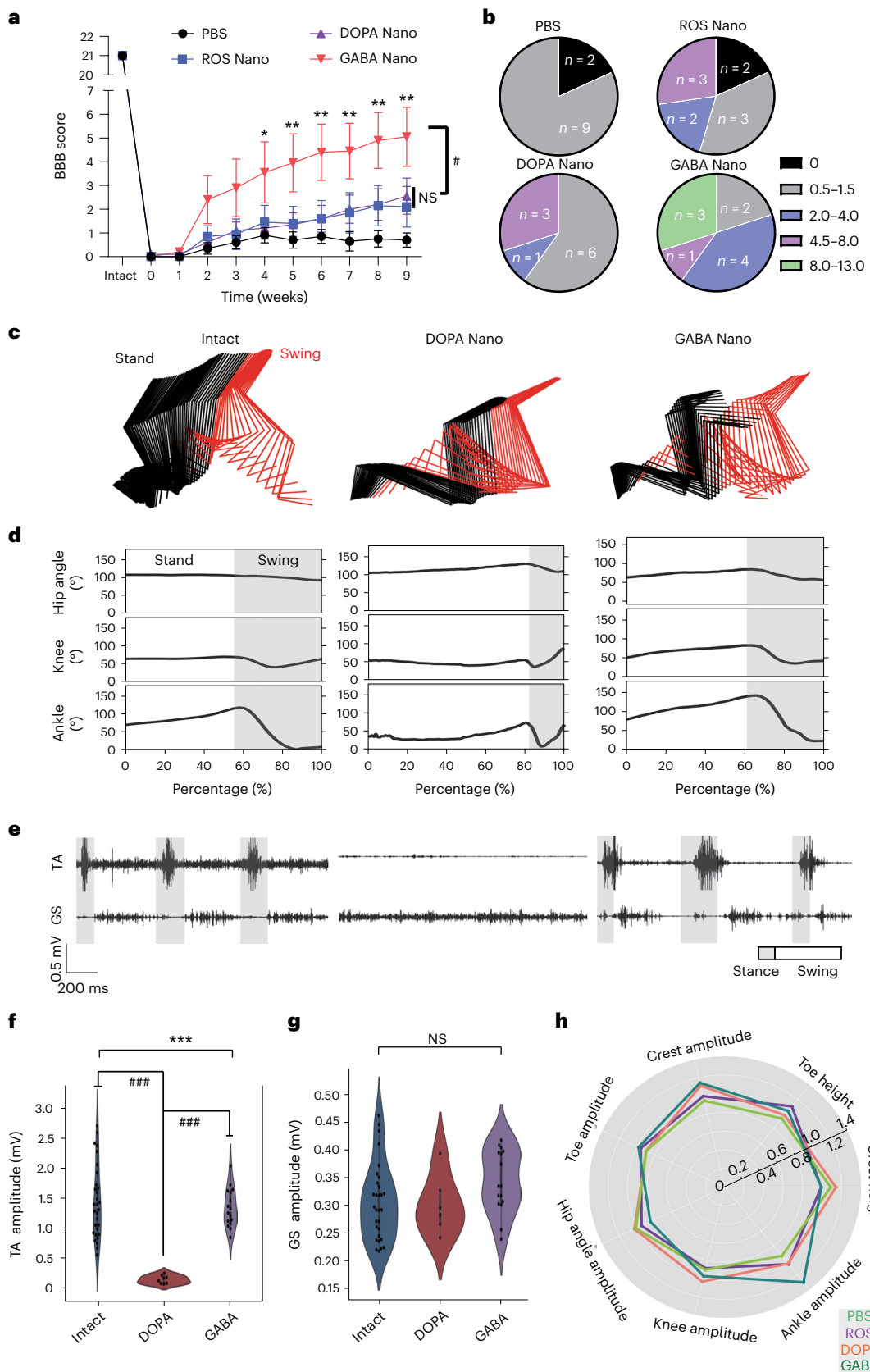
We speculated that the spinal cord circuits derived from spared descending axons or spared interneurons could not mediate hind-limb locomotion because the spinal interneurons were hyperactive after SCI and thus unable to efficiently relay signals from the brain to the lumbosacral central pattern generator. Therefore, we sought to assess whether neuron-targeting treatments would promote the integration of these circuits into the host spinal network and improve hind-limb locomotor function in contusion mode. Through histological analysis, we found that the GABA Nano and DOPA Nano treatments showed equivalent neuroprotective effects compared with the ROS Nano treatment in protecting the spared tissues, including the preserved axons and interneurons (Supplementary Figs. 7 and 8). Importantly, in our delivery system, the GABA-CLP or DOPA-CLP derived from CLP-257, could be hydrolysed within the targeted neuron and release CLP-257 for neuromodulation¹⁶. Interestingly, most of the rats treated with DOPA Nano displayed only ankle movements with a plateaued Basso, Beattie and Bresnahan (BBB) score of approximately 2 at the test time points (Fig. 5a,b), whereas rats treated with GABA Nano exhibited significantly improved hind-limb locomotor functions, performing hind-limb plantar placement or dorsal stepping at five weeks post injury ($P < 0.01$; Fig. 5a,b). More strikingly, three of the ten rats that were treated with GABA Nano recovered the ability to consistently take hind paw plantar steps with occasional weight support (Fig. 5b and Supplementary Video 1). These results suggested that GABA Nano treatment could markedly improve hind-limb motor function and weight-bearing stepping after severe SCI, and this was implicated as the limiting step for functional recovery in such a severe SCI model⁴². Detailed hind-limb kinematics revealed the following significant improvements with this GABA Nano treatment: (1) increased weight support (increased iliac crest height; Fig. 5d,h and Extended Data Fig. 5a); (2) increased maximum toe height and high aptitude (Extended Data Fig. 5c,d); and (3) strikingly increased ankle amplitude (Fig. 5d,h and Extended Data Fig. 5e–g). The individual diversity of functional recovery with treatment occurs possibly because the rescued tissues relevant to hind-limb locomotion are randomly presented in the injured rats. Moreover, the BBB scores were maintained for two weeks after the treatment was stopped (Supplementary Fig. 9), suggesting that the sustained functional recovery was due to GABA Nano treatment. To analyse the muscle activity of these rats,

Fig. 5 | GABA Nano treatment improves the recovery of hind-limb locomotor function in rats with severe contusive SCI. **a**, Weekly BBB scores of the rats treated with PBS, ROS Nano (10 mg kg⁻¹), DOPA Nano (10 mg kg⁻¹) or GABA Nano (10 mg kg⁻¹). Data are shown as the mean ± s.e.m. One-way analysis of variance (ANOVA) with Tukey's post hoc test was used for comparisons among multiple groups. $n = 10$ rats for each group. * $P < 0.05$, ** $P < 0.01$. GABA versus ROS 4 weeks, $P = 0.0488$; 5 weeks, $P = 0.0069$; 6 weeks, $P = 0.0142$; 7 weeks, $P = 0.0032$; 8 weeks, $P = 0.0019$; 9 week ANOVA for total $f = 4.727$, $P = 0.0070$; GABA versus PBS $P = 0.0023$; GABA versus ROS $P = 0.0101$. **b**, Pie graphs showing the distribution of BBB scores for rats with PBS, ROS Nano, DOPA Nano or GABA Nano treatments. **c**, Representative colour-coded stick views of kinematic hind-limb movement of intact rats or rats treated with DOPA Nano or ROS Nano. **d**, Representative curves of the hip, knee and ankle angles during a one-step cycle. **e**, Representative EMG data for the TA and GS muscles from the intact, DOPA Nano and GABA Nano groups. **f,g**, Quantitative analysis of signal amplitudes from TA and GS muscles

for rats with different treatments. Data are shown as the mean ± s.e.m. # and ### in f represent $P < 0.05$ and $P < 0.001$, respectively. One-way ANOVA with Tukey's post hoc test was used for comparisons among multiple groups. For the ANOVA for TA, total, $f = 22.99534$, $P = 7.610694 \times 10^{-8}$; GABA versus DOPA, $P = 1.315732 \times 10^{-6}$; intact versus DOPA, $P = 5.38020 \times 10^{-8}$. For the ANOVA for GS, total, $f = 2.050763$, $P = 0.139535$. Three animals from each group were recorded individually; $n = 12$ integral EMG data for intact group; $n = 5$ for DOPA Nano group and GABA Nano group. The violin plot centre indicates the median in all planes. Violin range covers 97.5th and 2.5th percentiles; extending whiskers show data distribution and probability density. Violin areas remain constant. Boxplot centre lines signify medians; boxes show first and third quartiles (Q1, Q3); whiskers extend from Q1 – 1.5 × IQR to Q3 + 1.5 × IQR where IQR is the interquartile range; outliers lie outside whiskers. * $P < 0.05$, ** $P < 0.01$. **h**, Well-rounded quantification of seven described behavioural features in animals subjected to the indicated treatments through a radar graph.

we recorded the electromyogram (EMG) of hind-limb muscles. We found that the ankle flexor tibialis anterior (TA) muscle and extensor gastrocnemius soleus (GS) muscle of rats treated with ROS Nano or DOPA Nano showed some activity during hind-limb joint movement,

while they were rarely active in rats treated with PBS (Fig. 5e). Interestingly, while the rhythm of the GS and TA muscles was compromised in rats treated with GABA Nano compared with intact rats, the GS muscles in rats treated with DOPA Nano showed a high amplitude without any



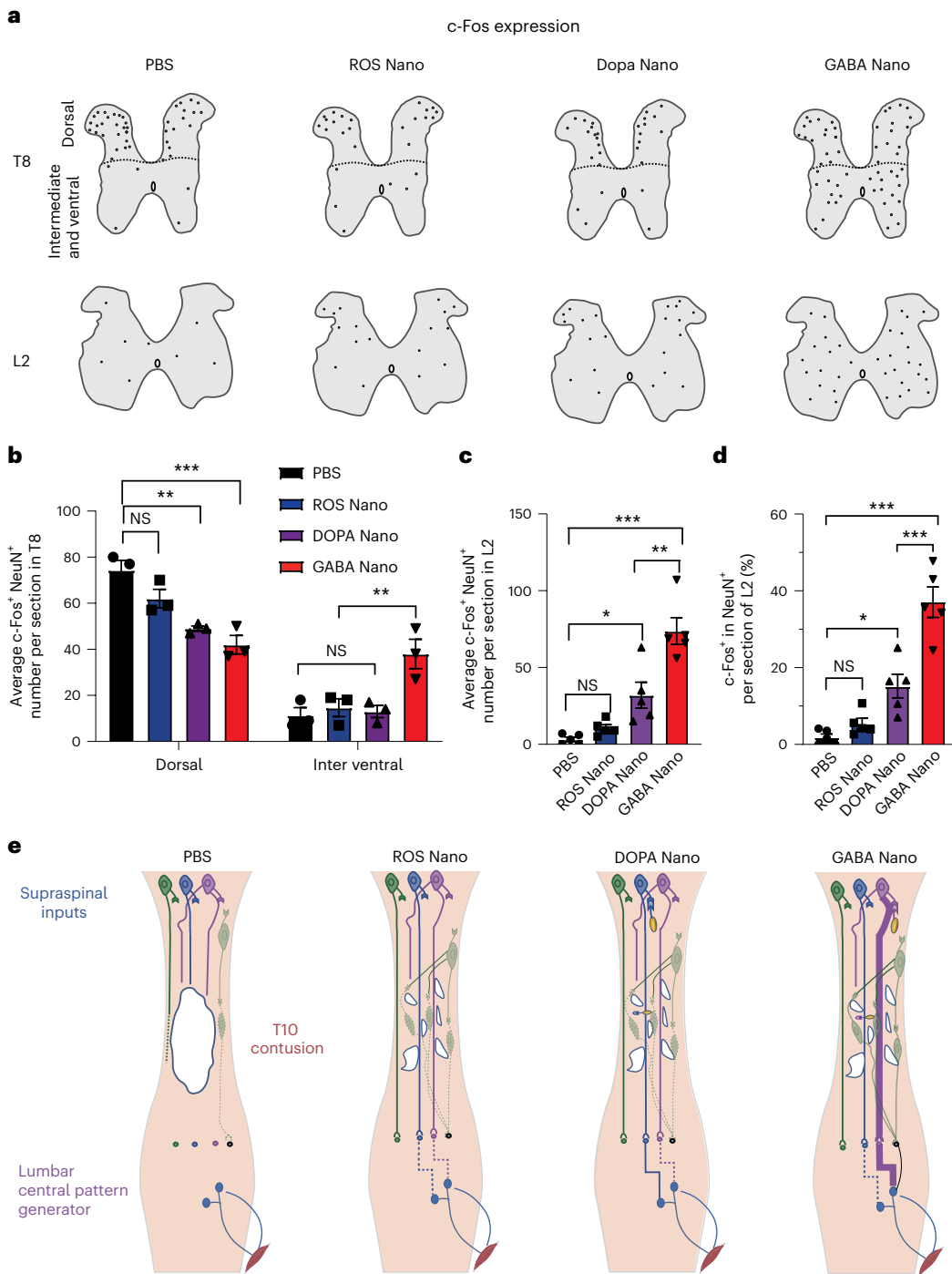


Fig. 6 | GABA Nano treatment rebalances neuronal activity and activates rescued residual spinal cord circuits to perform functions. **a**, Schematics of spinal cord cross-sections showing c-Fos expression (representing neuronal activity) patterns in T8 and L2 segments after 1 h of continuous locomotion of injured rats treated with PBS, ROS Nano, DOPA Nano or GABA Nano. Each spot represents a cell positively stained with both c-Fos and NeuN. Representative raw images are shown in Extended Data Fig. 6. **b**, Quantification of c-Fos⁺ neurons in dorsal or interventral T8 sections. Data are shown as the mean \pm s.e.m. One-way ANOVA with Tukey's post hoc test was used for comparisons among multiple groups, and two-tailed paired *t*-tests were used for comparisons between two groups. $n = 3$ rats for each group. For the dorsal, total $f = 15.72$, $r = 0.855$, $P = 0.0010$; DOPA versus PBS, $P = 0.0048$; GABA versus PBS, $P = 0.0009$. For the interventral, total $f = 8.598$, $r = 0.7633$, $P = 0.0070$; GABA versus PBS, $P = 0.0099$. * $P < 0.05$, ** $P < 0.01$, *** $P < 0.001$. The r value defines the strength of the relationship between the independent variable and the dependent variable.

in the quantitative model. **c**, Quantification of c-Fos⁺ neurons in L2 sections of all groups. Data are shown as the mean \pm s.e.m. One-way ANOVA with Tukey's post hoc test was used for comparisons among multiple groups. $n = 5$ rats for each group. * $P < 0.05$, ** $P < 0.01$. Total $f = 26.03$, $r = 0.8299$, $P < 0.0001$; DOPA versus PBS, $P = 0.0222$; GABA versus PBS, $P < 0.0001$; DOPA versus GABA, $P = 0.0011$. The r value defines the strength of the relationship between the independent variable and the dependent variable in the quantitative model. **d**, Quantification of the c-Fos⁺ percentage in NeuN⁺ cells in L2 sections of all groups. Data are shown as the mean \pm s.e.m. One-way ANOVA with Tukey's post hoc test was used for comparisons among multiple groups. $n = 5$ rats for each group. * $P < 0.05$, ** $P < 0.01$. Total $f = 35.62$, $r = 0.8698$, $P < 0.0001$; DOPA versus PBS, $P = 0.0126$; GABA versus PBS, $P < 0.0001$; DOPA versus GABA, $P = 0.0001$. The r value defines the strength of the relationship between the independent variable and the dependent variable in the quantitative model. **e**, Schematic of hypothetical effects of different treatments on the spinal cord after T10 contusion.

rhythm, which explains why they did not exhibit a normal gait (Fig. 5e and Extended Data Fig. 5h,i). Additional verifications (Supplementary Information and Supplementary Figs. 10 and 11) suggest that the functional recovery elicited by GABA Nano arises from its synergistic neuroprotective and neuromodulatory actions on surviving tissues.

GABA Nano treatment modulates local spinal cord circuits

It is known that reducing the excitability of inhibitory interneurons after SCI facilitates functional restoration¹². To assess whether GABA Nano treatment improved functional recovery through a similar mechanism, we used c-Fos protein immunoreactivity as a proxy to detect the neuronal activity of interneurons in the spinal cord. After walking on a treadmill for 1 h, the rats were killed, and their spinal cords were collected and stained with c-Fos and neuronal nuclear protein (NeuN) at nine weeks after SCI. As shown in Extended Data Fig. 6a,b, the c-Fos-positive (c-Fos⁺) cells in the spinal segments were largely costained with NeuN, suggesting that c-Fos immunostaining has a high specificity for neurons. Representative composites of c-Fos/NeuN double-positive cells are illustrated in Fig. 6a. In intact rats, c-Fos⁺ neurons were distributed uniformly in T8 and lumbar vertebra L2 spinal segments. However, in SCI rats treated with PBS or ROS Nano, c-Fos⁺ neurons accumulated primarily in the T8 dorsal horn and were rarely observed in L2 below the lesion. By contrast, GABA Nano treatment decreased the density of c-Fos⁺ neurons in the T8 dorsal horn and increased their presence in the intermediate and ventral spinal cord, similar to intact rats. GABA Nano treatment also significantly increased c-Fos⁺ neurons in L2 versus the controls. DOPA Nano treatment produced slight changes in the c-Fos⁺ neuron distribution of T8 compared to GABA Nano treatment (Fig. 6a–d and Extended Data Fig. 6). This may have been because dopaminergic neurons in the spinal cord are mainly responsible for physiological functions other than motor control⁴³. Conclusively, these findings suggest that the GABA Nano targeting treatment transforms the SCI-induced irregular activity pattern into a more physiological state and allows the spared circuits originating from preserved axons and interneurons to integrate into local spinal circuitry and re-engage the lumbosacral central pattern generator to perform functions (Fig. 6e).

Conclusion

This study provides a nanosystem for the delivery of drugs to the spinal cord in the treatment of SCI and presents a pioneering pharmacological approach to treat SCI by targeting specific neuron subtypes, protecting spared tissues and rebalancing neuromodulatory effects. This allows the spinal cord circuits originating from preserved axons and interneurons at the lesion site to properly integrate into the spinal network and trigger hind-limb locomotion. However, determining the quantifiable contributions of circuits derived from the spared axons or preserved interneurons driven by neuromodulatory effects is challenging due to current technology limitations, as seen in previous neuromodulation therapies⁴³. While the data suggest the drug targets specific inhibitory neurons, the particular types of neurons have yet to be identified. The relative contributions of preserved axons, interneurons and neuromodulation also remain to be quantified. Further research is needed to pinpoint how the drug exerts its effects before translating to clinical use. In addition, our data demonstrate that the nanodrug delivery system effectively transports the payload to the spinal cord when the BSCB is restored at 14 days post SCI, due to the ROS-responsive release of the drug. However, further investigation is needed to enhance the nanodrug's penetration in SCI patients who have not received timely treatment, as delivery efficiency declined after 14 days post injury, possibly due to decreased ROS levels in the lesion. This limitation arises because the nanodrug delivery strategy relies on BSCB disruption and ROS accumulation in the lesion. While CLP-257 has been demonstrated to penetrate the BSCB⁶, it is crucial to compare the delivery efficiency of

the nanodrug system with that of the bare CLP-257 drug before advancing to clinical trials.

Online content

Any methods, additional references, Nature Portfolio reporting summaries, source data, extended data, supplementary information, acknowledgements, peer review information; details of author contributions and competing interests; and statements of data and code availability are available at <https://doi.org/10.1038/s41565-023-01416-0>.

References

1. David, S. & Kroner, A. Repertoire of microglial and macrophage responses after spinal cord injury. *Nat. Rev. Neurosci.* **12**, 388–399 (2011).
2. Block, M. L., Zecca, L. & Hong, J. S. Microglia-mediated neurotoxicity: uncovering the molecular mechanisms. *Nat. Rev. Neurosci.* **8**, 57–69 (2007).
3. Uldreaj, A., Badner, A. & Fehlings, M. G. Promising neuroprotective strategies for traumatic spinal cord injury with a focus on the differential effects among anatomical levels of injury. *F1000Research* **6**, 1907 (2017).
4. Li, L. et al. A MnO₂ nanoparticle-dotted hydrogel promotes spinal cord repair via regulating reactive oxygen species microenvironment and synergizing with mesenchymal stem cells. *ACS Nano* **13**, 14283–14293 (2019).
5. Zhang, N. et al. A 3D fiber-hydrogel based non-viral gene delivery platform reveals that microRNAs promote axon regeneration and enhance functional recovery following spinal cord injury. *Adv. Sci.* **8**, e2100805 (2021).
6. Chen, B. et al. Reactivation of dormant relay pathways in injured spinal cord by KCC2 manipulations. *Cell* **174**, 521–535.e13 (2018).
7. Wilson, J. M., Blagovechtchenski, E. & Brownstone, R. M. Genetically defined inhibitory neurons in the mouse spinal cord dorsal horn: a possible source of rhythmic inhibition of motoneurons during fictive locomotion. *J. Neurosci.* **30**, 1137–1148 (2010).
8. Haring, M. et al. Neuronal atlas of the dorsal horn defines its architecture and links sensory input to transcriptional cell types. *Nat. Neurosci.* **21**, 869–880 (2018).
9. Brommer, B. et al. Improving hindlimb locomotor function by non-invasive AAV-mediated manipulations of propriospinal neurons in mice with complete spinal cord injury. *Nat. Commun.* **12**, 781 (2021).
10. Courtine, G. & Sofroniew, M. V. Spinal cord repair: advances in biology and technology. *Nat. Med.* **25**, 898–908 (2019).
11. Ramirez-Jarquin, U. N., Lazo-Gomez, R., Tovar, Y. R. L. B. & Tapia, R. Spinal inhibitory circuits and their role in motor neuron degeneration. *Neuropharmacology* **82**, 101–107 (2014).
12. Matsuya, R., Ushiyama, J. & Ushiba, J. Inhibitory interneuron circuits at cortical and spinal levels are associated with individual differences in corticomuscular coherence during isometric voluntary contraction. *Sci. Rep.* **7**, 44417 (2017).
13. Ramirez-Jarquin, U. N. & Tapia, R. Excitatory and inhibitory neuronal circuits in the spinal cord and their role in the control of motor neuron function and degeneration. *ACS Chem. Neurosci.* **9**, 211–216 (2018).
14. Rivera, C. et al. The K⁺/Cl⁻ co-transporter KCC2 renders GABA hyperpolarizing during neuronal maturation. *Nature* **397**, 251–255 (1999).
15. Boulenguez, P. et al. Down-regulation of the potassium-chloride cotransporter KCC2 contributes to spasticity after spinal cord injury. *Nat. Med.* **16**, 302–307 (2010).
16. Gagnon, M. et al. Chloride extrusion enhancers as novel therapeutics for neurological diseases. *Nat. Med.* **19**, 1524–1528 (2013).

17. Reinig, S., Driever, W. & Arrenberg, A. B. The descending diencephalic dopamine system is tuned to sensory stimuli. *Curr. Biol.* **27**, 318–333 (2017).
18. Li, Y. et al. Pericytes impair capillary blood flow and motor function after chronic spinal cord injury. *Nat. Med.* **23**, 733–741 (2017).
19. Sharples, S. A. et al. A dynamic role for dopamine receptors in the control of mammalian spinal networks. *Sci. Rep.* **10**, 16429 (2020).
20. Grillner, S. & Jessell, T. M. Measured motion: searching for simplicity in spinal locomotor networks. *Curr. Opin. Neurobiol.* **19**, 572–586 (2009).
21. Li, W. C. & Moult, P. R. The control of locomotor frequency by excitation and inhibition. *J. Neurosci.* **32**, 6220–6230 (2012).
22. Kiehn, O. Decoding the organization of spinal circuits that control locomotion. *Nat. Rev. Neurosci.* **17**, 224–238 (2016).
23. Jiang, X. C. et al. Neural stem cells transfected with reactive oxygen species-responsive polyplexes for effective treatment of ischemic stroke. *Adv. Mater.* **31**, e1807591 (2019).
24. Liu, P. et al. Biomimetic dendrimer-peptide conjugates for early multi-target therapy of Alzheimer's disease by inflammatory microenvironment modulation. *Adv. Mater.* **33**, e2100746 (2021).
25. Lu, Y. et al. Microenvironment remodeling micelles for Alzheimer's disease therapy by early modulation of activated microglia. *Adv. Sci.* **6**, 1801586 (2019).
26. Xu, W. et al. Increased production of reactive oxygen species contributes to motor neuron death in a compression mouse model of spinal cord injury. *Spinal Cord* **43**, 204–213 (2005).
27. Zhang, M. et al. Oxidation and temperature dual responsive polymers based on phenylboronic acid and N-isopropylacrylamide motifs. *Polym. Chem.* **7**, 1494–1504 (2016).
28. Lin, L. et al. Nanodrug with ROS and pH dual-sensitivity ameliorates liver fibrosis via multicellular regulation. *Adv. Sci.* **7**, 1903138 (2020).
29. Zhang, D., Fan, Y., Chen, H., Trepout, S. & Li, M. H. CO₂-activated reversible transition between polymersomes and micelles with AIE fluorescence. *Angew. Chem. Int. Ed.* **58**, 10260–10265 (2019).
30. Suk, J. S., Xu, Q., Kim, N., Hanes, J. & Ensign, L. M. PEGylation as a strategy for improving nanoparticle-based drug and gene delivery. *Adv. Drug Deliv. Rev.* **99**, 28–51 (2016).
31. Hu, J. et al. Long circulating polymeric nanoparticles for gene/drug delivery. *Curr. Drug Metab.* **19**, 723–738 (2018).
32. Zhang, Z. et al. Circulatory disturbance of rat spinal cord induced by occluding ligation of the dorsal spinal vein. *Acta Neuropathol.* **102**, 335–338 (2001).
33. Farrar, M. J., Rubin, J. D., Diago, D. M. & Schaffer, C. B. Characterization of blood flow in the mouse dorsal spinal venous system before and after dorsal spinal vein occlusion. *J. Cereb. Blood Flow. Metab.* **35**, 667–675 (2015).
34. Bartanusz, V., Jezova, D., Alajajian, B. & Digicaylioglu, M. The blood-spinal cord barrier: morphology and clinical implications. *Ann. Neurol.* **70**, 194–206 (2011).
35. Jin, L. Y. et al. Blood-spinal cord barrier in spinal cord injury: a review. *J. Neurotrauma* **38**, 1203–1224 (2021).
36. Zrzavy, T. et al. Acute and non-resolving inflammation associate with oxidative injury after human spinal cord injury. *Brain* **144**, 144–161 (2021).
37. Cooney, S. J., Zhao, Y. & Byrnes, K. R. Characterization of the expression and inflammatory activity of NADPH oxidase after spinal cord injury. *Free Radic. Res.* **48**, 929–939 (2014).
38. Bakh, N. A. et al. Glucose-responsive insulin by molecular and physical design. *Nat. Chem.* **9**, 937–943 (2017).
39. Chou, D. H. et al. Glucose-responsive insulin activity by covalent modification with aliphatic phenylboronic acid conjugates. *Proc. Natl Acad. Sci. USA* **112**, 2401–2406 (2015).
40. Ahuja, C. S. et al. Traumatic spinal cord injury. *Nat. Rev. Dis. Prim.* **3**, 17018 (2017).
41. Li, X. et al. The effect of a nanofiber-hydrogel composite on neural tissue repair and regeneration in the contused spinal cord. *Biomaterials* **245**, 119978 (2020).
42. Schucht, P., Raineteau, O., Schwab, M. E. & Fouad, K. Anatomical correlates of locomotor recovery following dorsal and ventral lesions of the rat spinal cord. *Exp. Neurol.* **176**, 143–153 (2002).
43. Qiao, Y. et al. Spinal dopaminergic mechanisms regulating the micturition reflex in male rats with complete spinal cord injury. *J. Neurotrauma* **38**, 803–817 (2021).

Publisher's note Springer Nature remains neutral with regard to jurisdictional claims in published maps and institutional affiliations.

Springer Nature or its licensor (e.g. a society or other partner) holds exclusive rights to this article under a publishing agreement with the author(s) or other rightsholder(s); author self-archiving of the accepted manuscript version of this article is solely governed by the terms of such publishing agreement and applicable law.

© The Author(s), under exclusive licence to Springer Nature Limited 2023

Methods

Animals and materials

All animal protocols were approved by the Institutional Animal Care and Use Committee and used following the provisions of the Zhejiang University Animal Experimentation Committee (ZJU202010110). Sprague–Dawley rats (200–250 g, female) were purchased from the Experimental Animal Center of the Zhejiang Academy of Medical Science. Chain transfer agent, 4-cyano-4-(phenylcarbonothioylthio) pentanoic acid; monomers, poly(ethylene glycol) methyl ether methacrylate (OEGMA; number-averaged molecular mass $M_n = 475$) and 3-acrylamidophenylboronic acid (BAA); and initiator, 2,2'-azobis (2-methylpropionitrile) (AIBN) were purchased from Aladdin Reagent. Monomers and initiators were purified by either recrystallization or filtration through an Al_2O_3 column to remove inhibitors. DOPA, GABA, *N,N'*-carbonyl diimidazole, fluorescein 5 (6)-isothiocyanate and Cy5.5 NHS ester were purchased from Sigma. Dialysis bags, PBS, Cell Counting Kit-8 (CCK-8) and 2',7'-dichlorofluorescin diacetate were obtained from Shanghai Yuanye Biological Technology. Hydrogen peroxide (H_2O_2), dimethyl sulfoxide (DMSO), tetrahydrofuran (THF), *N,N*-dimethylformamide diethyl acetal (DMF) and diethyl ether were also purchased from Aladdin Reagent. The KCC2 agonist CLP-257 was purchased from DC Chemicals. Methanol-d₄, chloroform-d and dimethyl sulfoxide-d₅ were purchased from Aladdin Reagent. RPMI 1640 medium, foetal bovine serum (FBS), horse serum and 1% penicillin/streptomycin were purchased from Gibco, and L-glutamine was obtained from Adamas. A live/dead viability/cytotoxicity kit was purchased from Thermo Fisher Scientific, and a bicinchoninic acid (BCA) protein assay kit and an enhanced chemiluminescence (ECL) kit were provided by Solabo.

Chicken anti-GFAP (Abcam (ab134436), 1:500), rabbit NF heavy polypeptide (Abcam (ab8135), 1:500), goat anti-5-HT antibody (Invitrogen (pa1-36157), 1:500), rabbit anti-inducible nitric oxide synthase (iNOS) (Abcam (ab283655), 1:200), goat anti-ionic calcium binding adapter molecule 1 (IBA1) (Abcam (ab5076), 1:500), rabbit anti-NeuN (Abcam (ab177487), 1:500), goat anti-chicken immunoglobulin of yolk (heavy and light chains) (IgY (H+L)) (Abcam (ab150172), 1:500) and rabbit anti-GABA antibody (Abcam (ab216465), 1:200) were obtained from Abcam. Rabbit anti-transforming growth factor-β (TGF-β) (A15103), rabbit anti-B-cell lymphoma-2 (Bcl-2) (A0208) and rabbit anti-BCL2-associated X (Bax) (A0207) were obtained from Abclonal. Mouse anti-DOPA antibody (sc-374376, 1:200) was obtained from Santa Cruz Biotechnology. Rabbit anti-c-Fos (226004, 1:200) was purchased from Synaptic Systems. Donkey anti-chicken secondary antibody conjugated with Alexa Fluor 488 (1:500), donkey anti-rabbit immunoglobulin g (IgG (H+L)) highly cross-adsorbed secondary antibody conjugated with Alexa Fluor 555 (1:500), donkey anti-mouse secondary antibody conjugated with fluorescein 5 (6)-isothiocyanate 493 (1:500) and rabbit anti-goat secondary antibody conjugated with cyanine 3 (Cy3) (1:500) were purchased from Abcam. Donkey anti-rabbit secondary antibodies conjugated with horse-radish peroxidase (HRP) (1:10,000) were purchased from Abclonal. The adenovirus-associated viruses AAV2/9-hSyn-mCherry were generated by the viral core of Zhejiang University, and their titre was adjusted to 1×10^{13} copies per millilitre for injection.

Characterization

TEM imaging was conducted using a Tecnai Spirit electron microscope at 120 kV (Thermo). The hydrodynamic radius and zeta potential were characterized via dynamic light scattering using a Litesizer 500 (Anton Paar). The ¹H-NMR spectra were obtained by an Avance III 500 MHz (Bruker). The number-averaged molecular mass (M_n) was characterized by gel permeation chromatography, which was performed on a modular system composed of a Waters 515 high-pressure liquid chromatographic pump, with DMF as the eluent (1 ml min⁻¹), and a Viscotek LR40 refractometer. All samples (5 mg) for analysis were dissolved in ~1 ml of DMF and filtered through 0.2 μm filters prior to injection.

Synthesis and characterization of GABA-CLP and DOPA-CLP

To synthesize GABA-CLP, CLP-257 (30.7 mg, 0.1 mmol, 1 equiv.) was dissolved in DMSO (2 ml), and then *N,N'*-carbonyl diimidazole (20 mg, ~0.12 mmol, 1.2 equiv.) was added to the solution. After 30 min, GABA (11 mg, 0.1 mmol, 1 equiv.) was added to the mixture for the formation of modified CLP. The mixture was then precipitated several times in deionized water followed by washing several times with methanol for purification. Finally, the pale-yellow solids powder (GABA-CLP) were collected after recrystallization or freeze drying and were characterized by ¹H-NMR. To identify GABA-CLP targeting and metabolic processes, fluorescent labelling was performed. A similar procedure was used to prepare GABA-Cy5.5 using Cy5.5 instead of CLP-257. DOPA-CLP was obtained by a similar synthetic procedure with DOPA (19 mg, 0.1 mmol, 1 equiv.) instead of GABA. For fluorescent observation, DOPA-Cy5.5 was prepared by a similar procedure with Cy5.5 instead of CLP-257.

Synthesis and characterization of copolymer

The copolymers (poly(OEGMA)_x-b-(BAA)_y, named POEGMA-BAA) were prepared using reversible addition–fragmentation chain transfer polymerization. To optimize the molecular weight of the copolymer, four other kinds of micelles with copolymers of POEGMA₁₅-BAA₂, POEGMA₃₀-BAA₂, POEGMA₄₀-BAA₂ and POEGMA₅₀-BAA₂ were prepared.

A representative synthetic procedure for POEGMA₃₀-BAA₂ was as follows: first, chain transfer agent (28 mg, 0.1 mmol, 1 equiv.), OEGMA (1.66 g, 3.5 mmol, 35 equiv.) and AIBN (1.6 mg, 0.01 mmol, 0.1 equiv.) were dissolved in 2 ml DMF under an atmosphere of N₂ in a Schlenk tube. The mixture solution was degassed by three repeated freeze–evacuate–thaw cycles to remove the dissolved oxygen. The polymerization was carried out at 70 °C for 12 h. The mixture was stopped by exposure to air and precipitated in diethyl ether three times to obtain a red oil named POEGMA. Then, POEGMA (0.72 g, ~1 equiv.), BAA (3 mg, 0.016 mmol, 3 equiv.) and AIBN (0.8 mg, 0.005 mmol, 1 equiv.) were dissolved in 1.5 ml DMF under an atmosphere of N₂, frozen in liquid nitrogen and degassed for 30 min to remove dissolved oxygen. The polymerization was carried out at 70 °C and was stopped after 10 h by exposure to air. The mixture was precipitated in diethyl ether three times to obtain copolymer POEGMA-BAA₂ as an orange oil. The obtained POEGMA and POEGMA-BAA₂ were characterized by ¹H-NMR. Copolymers (POEGMA₁₅-BAA₂, POEGMA₃₀-BAA₂, POEGMA₄₀-BAA₂ and POEGMA₅₀-BAA₂) with various molecular weights were obtained using different OEGMA and BAA monomer feeding ratios.

To prepare the treatments for the non-neuroprotection group, boron-free amphiphilic polymers were synthesized as follows: first, POEGMA was synthesized using the method above. Then, POEGMA (0.72 g, ~1 equiv.), *N*-phenylacrylamide (PAm; 3 mg, 0.021 mmol, 4 equiv.) and AIBN (0.8 mg, 0.005 mmol, 1 equiv.) were used to obtain POEGMA₃₀-PAm₂ by similar process as in POEGMA-BAA₂ synthesis. The obtained POEGMA₃₀-PAm₂ was characterized by ¹H-NMR.

Synthesis and characterization of micelles and nanoparticles

The micelles and nanoparticles were prepared by membrane dialysis⁴⁴. Copolymers with different molecular weights (150 mg) were dissolved in 10 ml DMSO and pushed through a syringe pump to produce self-assembled micelles in 5 ml deionized water. Micelles were obtained by dialysis against water for 24 h using porous dialysis tubing (molecular weight cut-off, 3,500), which completely removed DMSO. As a result, micelles formed from POEGMA₃₀-BAA₂ that had good dispersibility and an appropriate size were used in the following experiments.

Then, we encapsulated the prodrug of GABA-CLP or DOPA-CLP in the micelles for sustained drug release. POEGMA₃₀-BAA₂ (100 mg) and GABA-CLP or DOPA-CLP (50 mg) were dissolved in 10 ml DMSO. The mixture underwent the same procedure for micelle formation and DMSO removal described above. The obtained nanoparticles with prodrugs were named GABA Nano or DOPA Nano, respectively.

The GABA Nano and DOPA Nano that were used for fluorescence observation were prepared using GABA-Cy5.5 and DOPA-Cy5.5 for micelle formation instead of GABA-CLP and DOPA-CLP. In all, the following types of micelles were prepared: CLP-257-binding GABA-targeting micelles (GABA Nano), CLP-257-binding DOPA-targeting micelles (DOPA Nano), Cy5.5-binding GABA-targeting micelles (GABA Nano@Cy5.5) and Cy5.5-binding DOPA-targeting micelles (DOPA Nano@Cy5.5). Micelles formed by POEGMA₃₀-BAA₂ without drug loading were used as controls (ROS Nano). The critical micelle concentration, particle size, size distribution and zeta potential of the micelles and nanoparticles were determined using dynamic light scattering. To prepare the treatments for the neuromodulation-only group, nanoparticles were assembled from POEGMA₃₀-PAm₂ loaded with GABA-CLP. POEGMA₃₀-PAm₂ (100 mg) and GABA-CLP (50 mg) were dissolved in 10 ml DMSO. The obtained nanoparticles with prodrugs were labelled GABA Nano without neuroprotection. The morphology of the micelles and nanoparticles was characterized by TEM.

Release and degradation of ROS Nano by ROS stimulation

To characterize the features of ROS Nano under ROS stimulation, micelles (ROS Nano@Nile Red) were formed by POEGMA₃₀-BAA₂ (100 mg) and Nile red (40 mg) using the membrane dialysis method. Then, ROS Nano@Nile Red (~5 mg, containing 1 mg Nile red) was dissolved in H₂O₂ solutions with different concentrations (0, 50, 100 and 500 mM; 1 ml). The fluorescence intensity was measured at certain intervals, and the release profiles of ROS Nano with ROS stimulation were obtained according to the changes in fluorescence intensity. The morphological changes in ROS Nano in H₂O₂ solution (500 mM, 5 mg ml⁻¹) were characterized by a TEM microscope after oxidation for 1 h and 2 h.

Biocompatibility characterization

PC12 cells were cultured in RPMI 1640 medium supplemented with 5% FBS, 10% horse serum, 1% penicillin/streptomycin and 2 mM L-glutamine for proliferation. A standard CCK-8 assay was used to test cell toxicity. Briefly, suspended PC12 cells were seeded in 96-well cell culture plates (10,000 cells per well) and cultured in medium for 24 h. Then, ROS Nano, GABA Nano or DOPA Nano was added to the medium at concentrations of 0, 31, 63, 125, 250 and 500 µg ml⁻¹, and the samples were maintained for 24 h. After washing twice with PBS, 100 µl CCK-8 solution was added to each well, and the samples were incubated for another 2 h. The absorbance of each well was measured with 450 nm laser excitation, and the cell survival ratio was obtained in relation to that in the control groups.

According to the manual, viability was further investigated with a LIVE/DEAD viability/cytotoxicity kit. Briefly, cells treated with ROS Nano for 24 h were stained with 100 µl of 2 mM acetyl methoxy methyl ester (calcein AM) or 1.5 mM propidium iodide for 15 min at 37 °C in ×1 buffer and were then observed by inverted fluorescence microscopy (Olympus IX53).

Cell protection from ROS damage by ROS-responsive nanodrugs

To assess whether ROS-responsive nanodrugs can protect cells from ROS-induced apoptosis, medium containing H₂O₂ (100 µM) was used in cell culture. ROS Nano, GABA Nano or DOPA Nano was added to the medium at concentrations ranging from 0 to 1 mg ml⁻¹. After 24 h, the cells were washed twice with PBS and tested by CCK-8 assay.

Lipopolysaccharide-containing medium was used to simulate the ROS microenvironment in damaged tissues. Cells were cultured with lipopolysaccharide-containing medium (100 ng ml⁻¹) and treated with ROS Nano, GABA Nano or DOPA Nano (250 µg ml⁻¹) for 6 h. Then, 2',7'-dichlorofluorescin diacetate detection was performed by adding 10 µM 2',7'-dichlorofluorescin diacetate for 20 min at 37 °C, followed by inverted fluorescence microscope observation.

Surgical procedures

The spinal cord contusion injury model⁴⁵ was established by an infinite vertical impactor (68099, RWD Life Science). To expose the dorsal surface of the spinal cord, laminectomy was performed at the tenth thoracic vertebral level (T10–T11) after the rats had been anaesthetized with pentobarbital sodium (0.5 ml per 100 g). The spinal cord contusion was performed by smashing an impactor tip into the spinal cord to a depth of 2.5 cm using a 3-mm-diameter cylinder at a velocity of 2.5 m s⁻¹. Following surgery, the muscles and skin were sutured, and bladder care was provided twice daily until spontaneous voiding resumed. The rats used for the experiments were distributed into the following groups: PBS group, ROS Nano group, GABA Nano group and DOPA Nano group. For the first week after SCI, 200 µl of each Nano solution (10 mg ml⁻¹) or PBS was administered by tail vein injection every 48 h. During the following weeks, 200 µl of each Nano solution (10 mg ml⁻¹) was administered via tail vein injection once a week.

A T10 complete crush model was performed⁶. Briefly, a midline incision was made over the thoracic vertebrae, followed by a T10 laminectomy. A complete T10 crush was then carefully conducted using surgical forceps (width, 0.1 mm). After surgery, the muscles and skin were sutured and bladder care was provided.

To independently assess the neuromodulatory function of GABA Nano, we conducted an additional experiment using GABA Nano without neuroprotection as the experimental group (Sprague Dawley (SD) rat, n = 10), a ROS Nano group (SD rat, n = 10) and PBS (SD rat, n = 10) as the control group. The spinal cord contusion injury model was established as previously described. In the additional experiment, the experimenter intravenously administered the drug to the rats at a dose of 10 mg kg⁻¹ at consecutive time points after SCI. Another group of examiners blinded to the drug treatment groups analysed the rats' histology and hind-limb locomotion performance.

To perform anterograde tracing of propriospinal axons, rats underwent dorsal laminectomy at the eighth thoracic vertebral level (T7–T8 spinal cord). Then, according to the method described in previous literature⁴⁵, AAV2/9-hSyn-mCherry was injected into the T7–T8 spinal cord of rats two weeks before termination. Histological assessment was performed nine weeks after injury.

Histology and 3D reconstruction

To collect spinal cord tissues, the rats were deeply anaesthetized with pentobarbital sodium (0.5 ml per 100 g) and intracardially perfused with 4% paraformaldehyde at the ninth week post injury. Before embedding, the fixed spinal cords were immersed in 30% and 15% sucrose solutions for dehydration. Spinal cord blocks were sectioned using a cryostat (CryoStar NX50; Thermo) and thaw-mounted onto Super Frost Plus slides (Fisher Scientific). Then, these sections were processed for immunohistochemistry assessments. After blocking with PBS containing 5% donkey serum and 0.3% Triton X-100 surfactant, spinal cord sections were incubated with primary antibodies. Then, the sections were washed three times with PBS and incubated with the appropriate secondary antibodies. Finally, the section slides were observed by confocal laser scanning microscopy (A1Ti, Nikon). The landmarks of the rat spinal segments were identified by the book *The Spinal Cord* by C. Watson et al.⁴⁶.

Quantitative analyses of the cavity volume of injured spinal cord tissues were performed⁴⁷. Briefly, serial spinal cord cross-sections equally spaced 150 µm apart were stained with H&E and imaged by a virtual digital slice scanning system (VS120, Olympus) for 3D reconstruction. A 7.5 mm spinal cord segment, containing the focal point of injury, was used in conjunction with 50 cross-sectional slices to generate 3D images. All 3D images were created by Amira software, and the cavity and pathological tissue were quantified. Similarly, this method was also used to analyse and quantify the preserved neurons and axons in and around the injury sites of the spinal cord. Briefly, serial spinal cord cross-sections with a thickness of 30 µm, equally spaced about

150 μm apart (one of every six sections was selected), were stained with proper antibody and DAPI. These sections were then imaged using a virtual digital slice scanning system (VS120, Olympus). To generate 3D images, a 7.5 mm spinal cord segment containing the focal point of injury was sectioned and stained. The number of preserved neurons was quantified using Amira software, and a 3D model was created. The total number of surviving neurons at the injury sites was estimated by multiplying the achieved numbers by six.

Toxicity and anti-apoptosis function of ROS Nano *in vivo*

To assess ROS nanotoxicity, rats treated with ROS Nano or PBS at the time points described previously were anaesthetized and perfused with 4% paraformaldehyde on day 7 post injury. Sections of the heart, liver, spleen, lung, kidney and brain were collected and subjected to H&E staining for the observation of tissue morphologies. To assess the anti-apoptosis function of ROS Nano, spinal cord segments 1–2 mm rostral and caudal to the injury site were dissected. Then, the tissue was homogenized using a homogenate in lysis buffer and centrifuged at 12,000g and 4 °C for 10 min to obtain the supernatant. The total protein content was measured with a BCA protein assay kit. Forty micrograms per sample protein was loaded onto a 10% polyacrylamide gel, separated by sodium dodecyl sulphate–polyacrylamide gel electrophoresis, and transferred to polyvinylidene fluoride membranes. After blocking with 5% skimmed milk in PBST buffer for 1 h at room temperature, membranes were placed in primary antibody (rabbit anti-TGF- β , rabbit anti-Bcl-2, rabbit anti-Bax, 1:1,000 dilution by 5% bovine serum albumin (BSA)) overnight at 4 °C. After washing with PBST three times, the membrane was incubated with a secondary antibody (goat anti-rabbit HRP) for 1 h at room temperature. Then, protein signals were visualized using an ECL kit and measured by Image Lab Software provided by Bio-Rad.

Cytokine/chemokine analysis

In this study, the examiners were blinded to the drug treatments, and 10 mg kg⁻¹ ROS Nano or PBS was intravenously administered to rats at serial time points after SCI. Rats were killed on day 7 after SCI ($n = 3$). To assess the cytokine/chemokine modulation of ROS Nano, spinal cord segments 1–2 mm rostral and caudal to the injury site were dissected. To assess systemic cytokine/chemokine expression, blood was collected from the orbital vein. An array of cytokine/chemokine analyses in both the spinal cord and serum were performed by an independent institution. The cytokines/chemokines were quantified using a MILLIPLEX MAP Rat Cytokine/Chemokine Magnetic Bead Panel using the Luminex system following the manufacturer's instructions. To evaluate the degree of dispersion of samples, we used principal component analysis for all proteins to reduce the dimensionality of multiple variables to a few independent variables and exhibit the distribution of samples by the DESeq2 package. According to the protein expression levels of the two groups, difference analyses were performed with the DESeq2 package. In the difference detection process, the proteins with a \log_2 -fold change of >1 or <-1 and adjusted P value of <0.05 were considered differentially expressed proteins and used to generate volcano plots.

Drug targeting and distribution *in vivo*

To assess the targeting effect and biodistribution of nanodrugs, GABA Nano and DOPA Nano were administered via tail vein injection at 3 h post injury. At certain intervals (after injection for 3, 6, 24 and 48 h), the rats were deeply anaesthetized with pentobarbital sodium (0.5 ml per 100 g) and perfused intracardially with 4% paraformaldehyde. The heart, liver, spleen, lung, kidney, brain and spinal cord were collected and observed with an *in vivo* fluorescence imaging system (CRI Corporation, MK50101-EX). To assess the BSCB penetration capacity of the nanodrugs, ROS nanoinjection was performed in SCI rats at 4, 7 and 14 days post injury or in intact rats. Spinal cords were dissected at

6 h post injection and assessed by both an *in vivo* fluorescence imaging system and immunofluorescence histology.

Behavioural assessment

Behavioural assessment of rats was performed weekly in an open-field environment based on the original report of the BBB⁴⁸. Rats that showed BBB scores greater than 1.5 at one week following contusion were excluded from further analyses. To analyse the detailed hind-limb kinematics, the hind-limb movement of rats from different groups was recorded using the MotoRater (Vicon Motion Systems)⁴⁹. The stick views of the hind-limb and angle of rotation movements were obtained by MATLAB in a double-blinded manner.

The behavioural data were quantified in terms of seven features (maximal iliac crest height; crest height amplitude; maximal toe height; toe height amplitude; and hip, knee and ankle angle oscillations) within five groups (intact, PBS, ROS Nano, DOPA Nano and GABA Nano). These features were depicted in a radar graph.

Electromyography recording and data analysis

At nine weeks after SCI, bipolar electrodes were implanted for EMG recording⁵. Briefly, electrodes (AS632, Cooner Wire) were led by 25-gauge needles and inserted into the mid-belly of the medial GS and TA muscles of one hind-limb while rats were deeply anaesthetized. A common ground wire was inserted subcutaneously into the Achilles tendon area of the hind-limb. Wires were routed subcutaneously through the back to a small percutaneous connector securely cemented to the skull of the rat. EMG signals were acquired using a differential neuron signal amplifier (BTAM01L, Braintech) with 30 Hz to 2,000 Hz filtration, sampled at 30 kHz using a Neurostudio system (Braintech) and analysed by a custom MATLAB code.

In this study, the Poincaré analysis method was used to distinguish chaos from randomness by embedding datasets into a higher dimensional state space. For example, a time series of EMG peak signals was given as follows:

$$x_t, x_{t+1}, x_{t+2}, \dots, x_{t+n}.$$

To obtain a return map in its simplest form, we plotted $(x_t, x_{(t+1)})$, $(x_{(t+1)}, x_{(t+2)})$, $(x_{(t+2)}, x_{(t+3)})$ and so forth. The x_t is the signal value of the electromyographic signal x at time t , where $t = 1, 2, \dots, t+n$ are time points separated by n time intervals from time t , where $n = 1, 2, \dots$. In this way, the interval length between two EMG peak signals in a series could be clearly represented in the plot, facilitating rhythm quantification among different groups (intact, PBS, ROS Nano, GABA Nano and DOPA Nano). Finally, we obtained both amplitude and rhythm information by analysing the EMG data.

Statistical analysis

For statistics, data were analysed using Graph Prism 8 (v.8.3.0, GraphPad Software), Python SciPy (v.1.4.1) and R language package (v.3.4.1-x64). For microscopy, images were analysed using Fiji (Windows 64, v.1.51; National Institutes of Health). Three-dimensional images were created by Amira software (v.6.01). EMG data analysis and behavioural assessment were done using MATLAB (v.2020b). In our study, all statistical analyses were performed against the control for single-factor analysis. For example, at the same treatment time point, we compared the treatment effect. Differences between the means of only two groups were analysed by Student's *t*-test. One-way ANOVA was used to compare the means of three or more groups. When there was a statistically significant difference among three or more sample means as determined by ANOVA, this comparison was followed by Tukey's post hoc analysis. A *P* value of less than 0.05 was considered significant.

Reporting summary

Further information on research design is available in the Nature Portfolio Reporting Summary linked to this article.

Data availability

The data to support the findings of this study are included in the paper, and further data are available from the corresponding author. Source data are provided with this paper.

References

44. Shi, Y. et al. Effective repair of traumatically injured spinal cord by nanoscale block copolymer micelles. *Nat. Nanotechnol.* **5**, 80–87 (2010).
45. Ye, J. et al. Rationally designed, self-assembling, multifunctional hydrogel depot repairs severe spinal cord injury. *Adv. Health Mater.* **10**, e2100242 (2021).
46. Watson, C. et al. in *The Spinal Cord Ch 15* (Academic Press, 2008).
47. Hong, L. T. A. et al. An injectable hydrogel enhances tissue repair after spinal cord injury by promoting extracellular matrix remodeling. *Nat. Commun.* **8**, 533 (2017).
48. Basso, D. M., Beattie, M. S. & Bresnahan, J. C. Graded histological and locomotor outcomes after spinal cord contusion using the NYU weight-drop device versus transection. *Exp. Neurol.* **139**, 244–256 (1996).
49. Wenger, N. et al. Spatiotemporal neuromodulation therapies engaging muscle synergies improve motor control after spinal cord injury. *Nat. Med.* **22**, 138–145 (2016).

Acknowledgements

We acknowledge the excellent technical staff at the Imaging Facility, Core Facility of Zhejiang University School of Medicine and Center of Cryo-Electron Microscopy of Zhejiang University for their assistance with confocal laser scanning microscopy and TEM. This study was supported by the Scientific and Technological Innovation 2030 Program of China, major projects (2021ZD0200408 to X.W.); the National Natural Science Foundation of China (81971866 to X.W.); the Science Fund for Distinguished Young Scholars of Zhejiang Province (LR20H090002 to X.W.); the Leading Innovative and Entrepreneur Team Introduction Program of Zhejiang (2019R01007 to X.W.); the

Fundamental Research Funds for the Central Universities (K20210195 to X.W.); and the National Major Project of Research and Development (2017YFA0104701 to B.Y.).

Author contributions

X.W. and Y.Z. conceptualized and designed the study. Y.Z., J.Y., W.C., X.C., L.L., B.G., S.J., H.Z., A.F., X.Q. and X.W. conducted the experiments. Y.Z., J.Y. and W.C. collected the data. Y.Z., J.Y., W.C., B.G., X.G., Z.W., Z.C., Z.Z., B.Y. and X.W. analysed and interpreted the data. Y.Z., X.W. and J.Y. drafted the paper. All authors critically revised the manuscript and approved the final version for submission.

Competing interests

Zhejiang University has filed a patent application related to this work, with X.W., Y.Z., J.Y., W.C., X.C., L.L. and B.G. listed as inventors. X.W. is a scientific cofounder of WeQure AI Ltd. All the other authors declare no competing interests.

Additional information

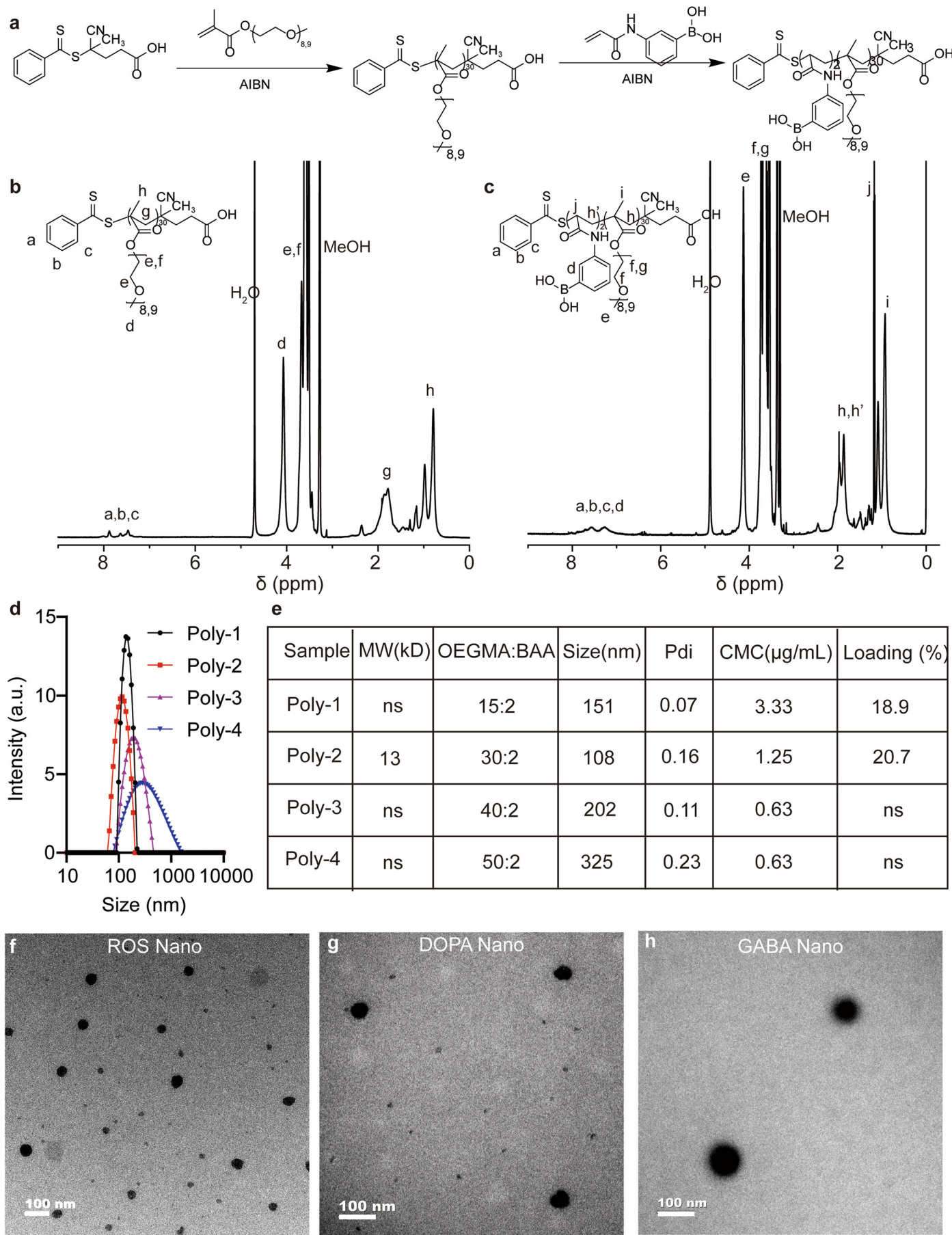
Extended data is available for this paper at <https://doi.org/10.1038/s41565-023-01416-0>.

Supplementary information The online version contains supplementary material available at <https://doi.org/10.1038/s41565-023-01416-0>.

Correspondence and requests for materials should be addressed to Xuhua Wang.

Peer review information *Nature Nanotechnology* thanks the anonymous reviewers for their contribution to the peer review of this work.

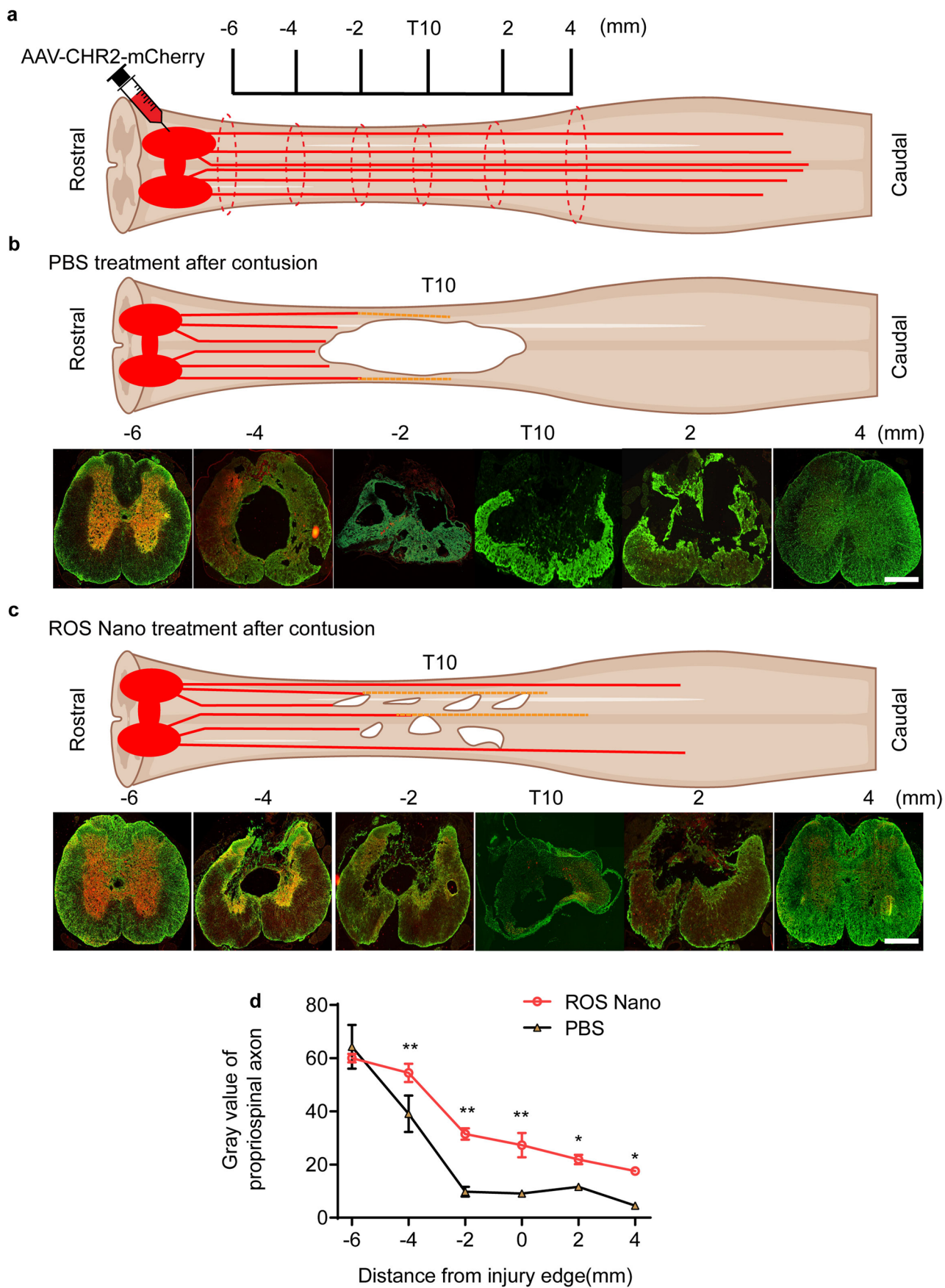
Reprints and permissions information is available at www.nature.com/reprints.



Extended Data Fig. 1 | See next page for caption.

Extended Data Fig. 1 | Synthesis and characterization of amphiphilic polymers and nanoparticles. **a**, The synthetic route of a representative amphiphilic polymer. **b, c**, Representative ^1H -NMR spectra of POEGMA₃₀ and POEGMA₃₀-BAA₂. **d, e**, Properties of nanoparticles with different compositions of

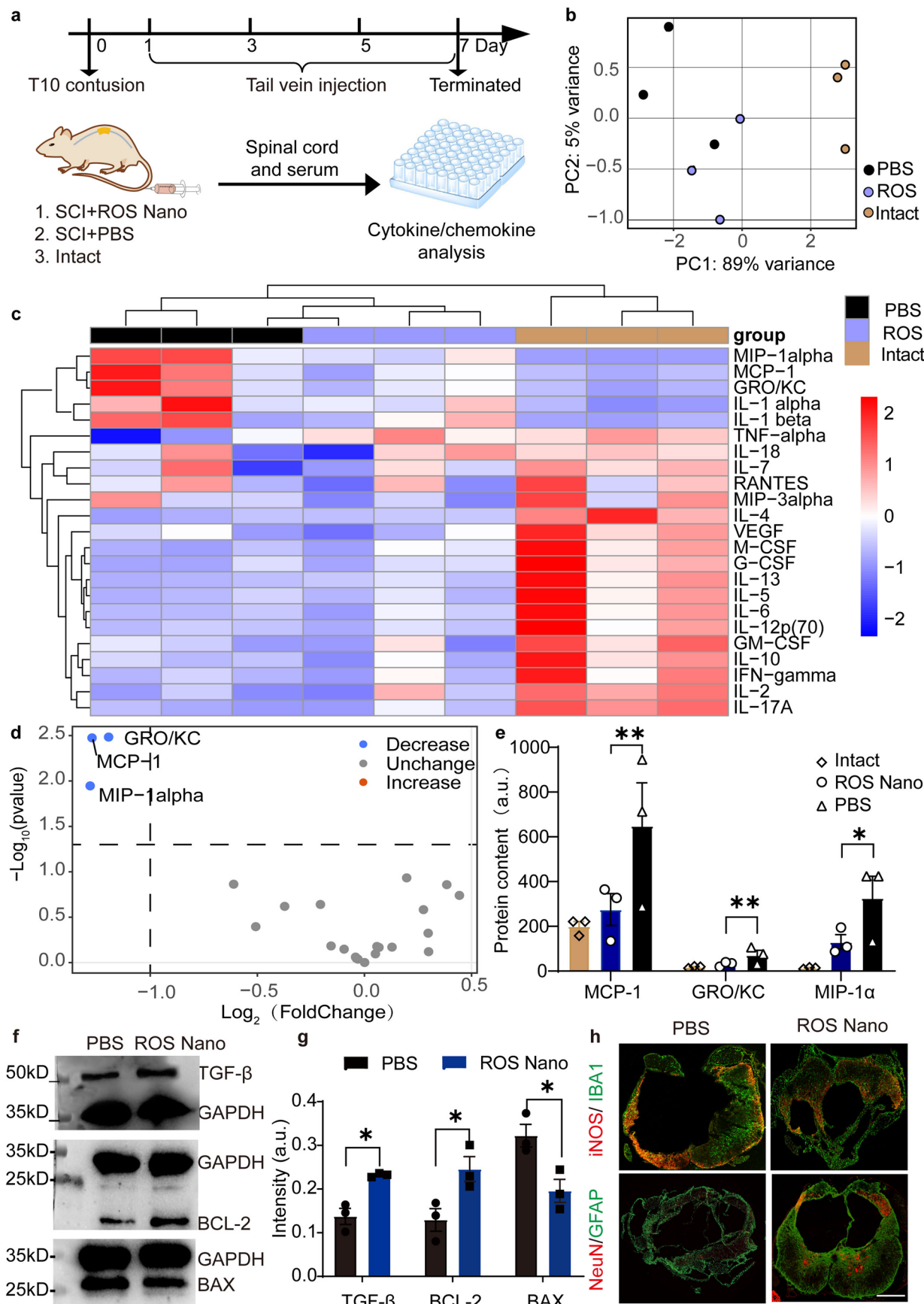
amphiphilic polymers. **f-h**, Representative TEM images of ROS Nano, DOPA Nano and GABA Nano. Scale bar, 100 nm. Independent experiments were repeated 3 times with similar results.



Extended Data Fig. 2 | See next page for caption.

Extended Data Fig. 2 | ROS Nano treatment protects spare propriospinal axons from secondary injury. **a**, Schematic diagram of the experimental design. **b, c**, Representative images of cross sections at certain sites stained by RFP (representing propriospinal axon, red) and GFAP (green) in PBS- or ROS Nano-treated rats. Scale bar, 500 μ m **d**, Quantitative analysis of propriospinal

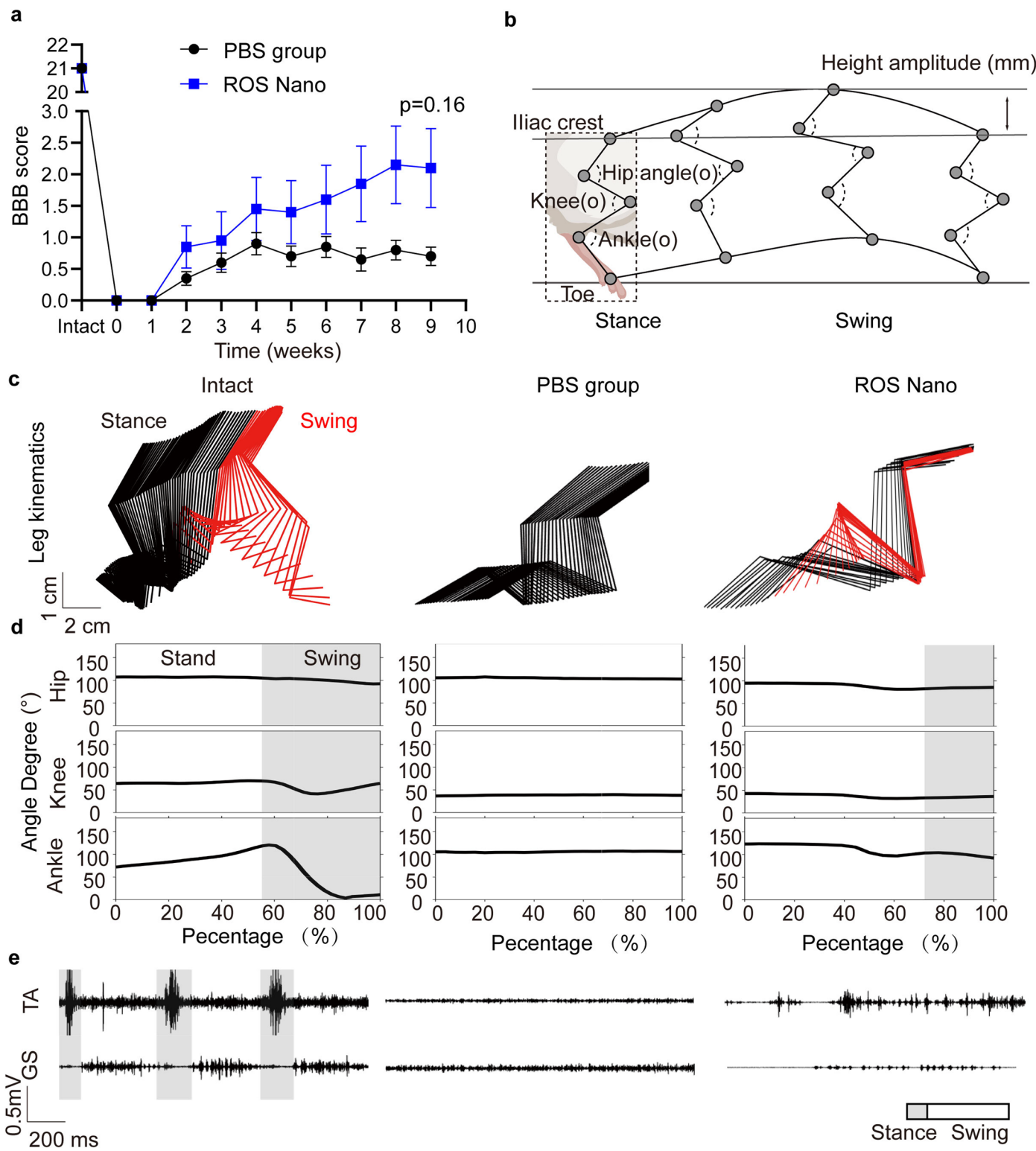
axons in rats treated with 9 weeks of ROS Nano or PBS. Data are shown as the mean \pm SEM. Two-tailed paired t tests were used for comparisons between two groups. n = 3 rats for each group. $p_{-4} = 0.0025$, $p_{-2} < 0.001$, $p_0 = 0.0155$, $p_2 = 0.004$, $p_4 = 0.0220$, * and ** indicate $p < 0.05$ and $p < 0.01$, respectively.



Extended Data Fig. 3 | See next page for caption.

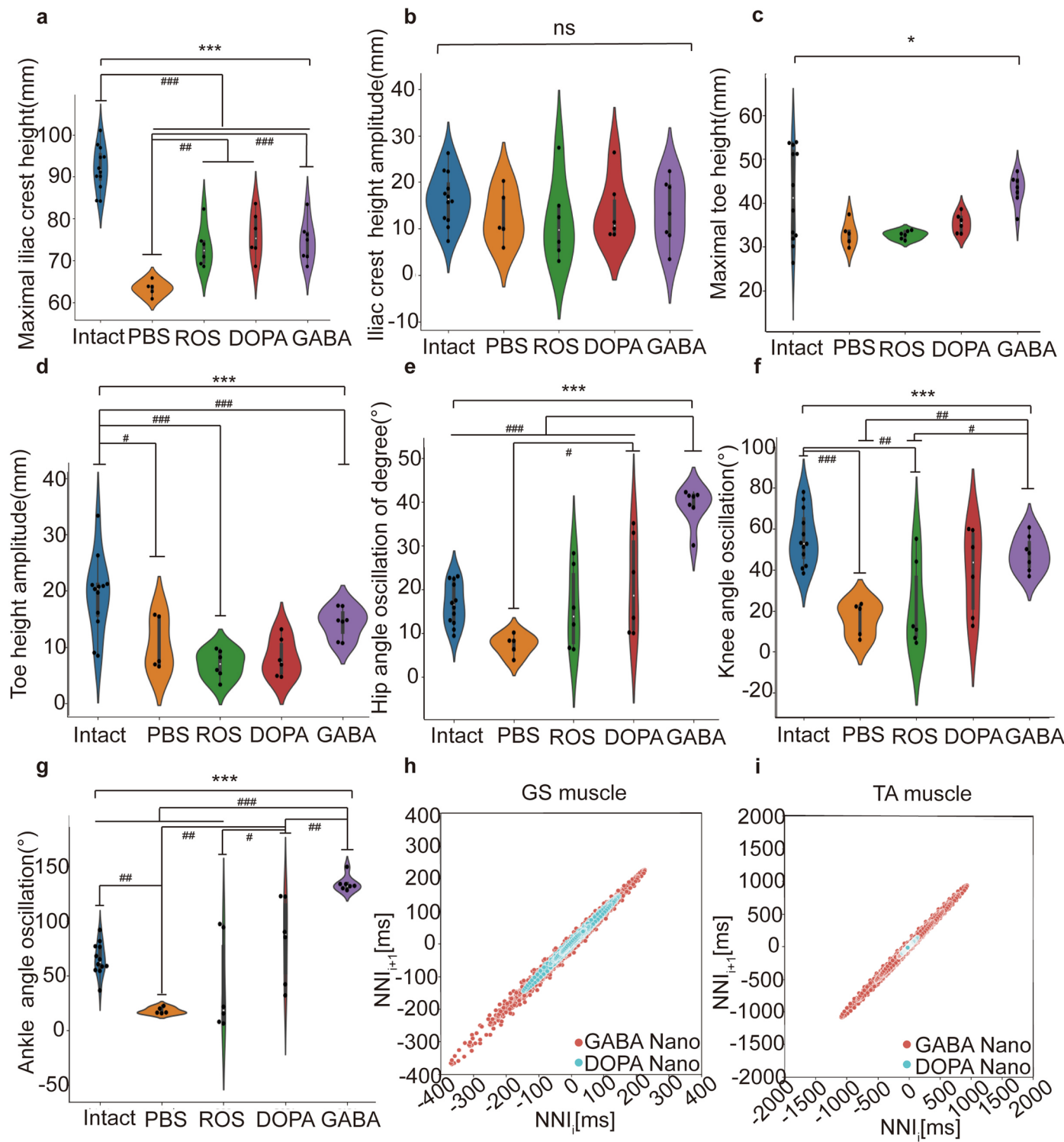
Extended Data Fig. 3 | ROS Nano treatment relieved excessive inflammation and reduced apoptosis in the injured spinal cord. **a**, Schematic diagram of the experimental design. **b**, Principal component analysis (PCA) of cytokine/chemokine expression in the spinal cord from 3 donors with different treatments. The effect of various ligand stimulations is largely described by PC1. **c**, Hierarchical clustering of the expression of cytokines/chemokines in the spinal cord from 3 donors with different treatments. The differential expression level is represented as the log₂-fold change (log₂[FC]) of normalized expression counts. Different treatments are arrayed by row and cytokine/chemokine by column. **d**, Volcano plot of cytokines/chemokines between the ROS Nano and PBS groups. Thresholds: -Log₁₀ adjusted p value < 0.05, Log₂[FC] > 1. All data is presented in supplementary table. **e**, Quantitative analyses of MCP-1, GRO/KC and MIP-1 α

expression in the spinal cord after different treatments. n = 3 rats for each group. One-way ANOVA with Tukey's post hoc test was used for comparisons among multiple groups. Two-tailed unpaired t tests were used for comparisons between two groups. ROS vs PBS (MCP-1, p = 0.00335), (GRO/KC, p = 0.00328) and (MIP-1 α , p = 0.0113). * indicates p < 0.05 and ** indicates p < 0.001. Data are shown as the mean \pm SEM. **f, g**, Representative immunoblots and quantitative analyses of TGF- β (p = 0.0419), BCL-2 (p = 0.0439) and BAX (p = 0.0271) expression in the injury site 1 week after PBS or ROS Nano (10 mg/kg) treatment. n = 3 rats for each group. Two-tailed unpaired t tests were used for comparisons between two groups. * indicates p < 0.05. Data are shown as the mean \pm SEM. **h**, Representative images of transverse sections at the epicenter of an injury stained with iNOS (red)/IBA1 (green) or NeuN (red)/GFAP (green) after 4 weeks of treatment.



Extended Data Fig. 4 | The preserved spinal cord circuits mediate limited hindlimb locomotor functional recovery. **a**, Weekly BBB scores of the experimental rats treated with PBS or ROS Nano. Data are shown as the mean \pm SEM. Two-tailed paired t tests were used for comparisons between two groups. n = 10 rats for each group. **b**, A simplified stick mode shows a one-step cycle of one intact hindlimb while the rat freely walked. The model also shows the quantification of the hip, knee and ankle angles and iliac crest height amplitudes

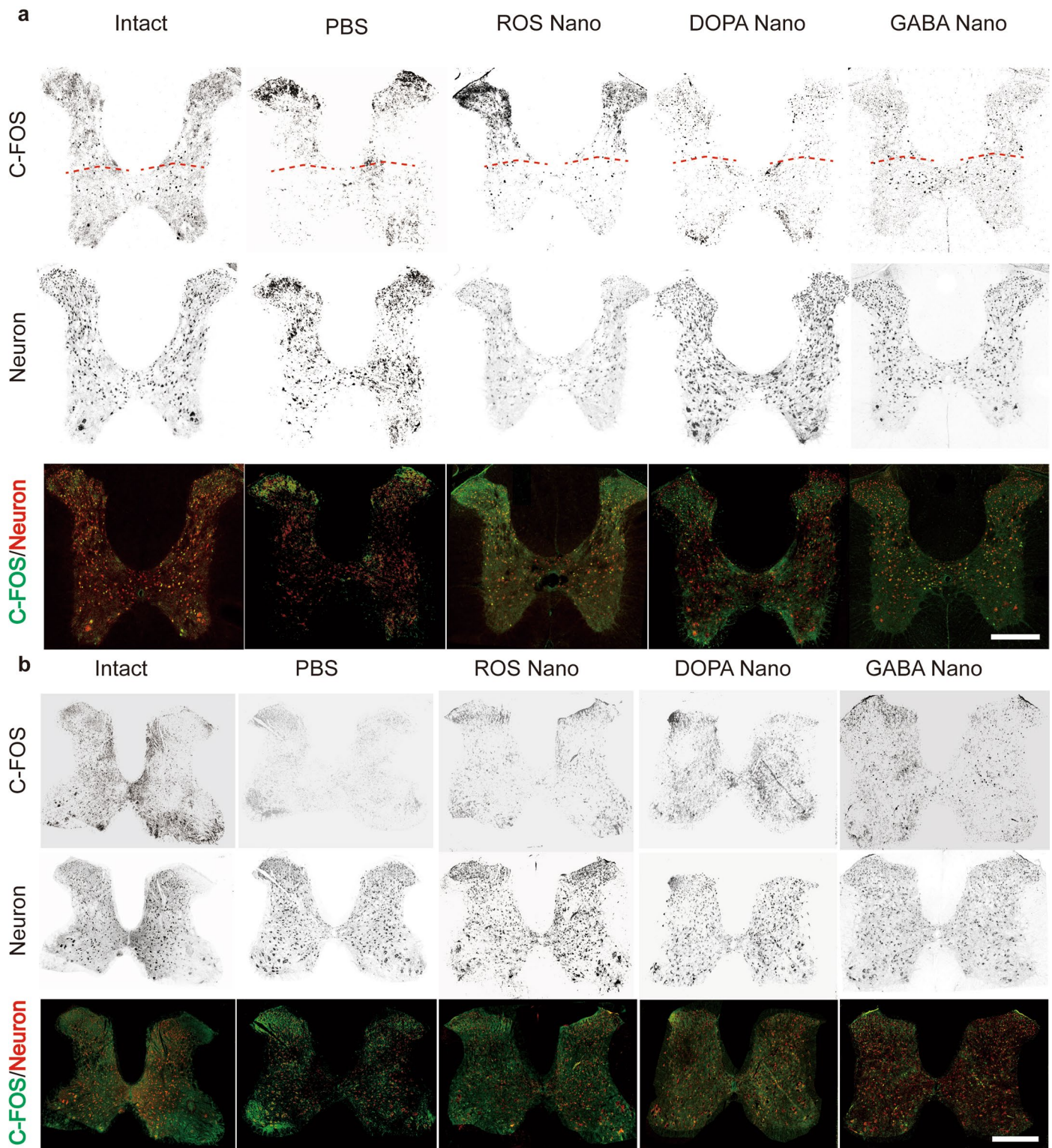
during the cycle. **c**, Representative color-coded stick views of kinematic hindlimb movement of intact, PBS-treated or ROS Nano-treated rats. **d**, Representative curves of hip, knee and ankle angles during the one-step cycle. **e**, Representative EMG of the TA and GS muscles of rats with different treatments. Gray bars, stance; white bars, swing. Independent experiments were repeated 3 times with similar results.



Extended Data Fig. 5 | See next page for caption.

Extended Data Fig. 5 | Detailed statistical analysis of the hindlimb movement of rats with different treatments. **a**, Quantification of the average maximal iliac crest height among groups. **b**, Quantification of the iliac crest height amplitude among rats with different treatments. One-way ANOVA with Tukey's post hoc test was performed for comparisons among multiple groups (*) and comparisons within groups (#) for the data shown in the violin plot. ***p (or ###p) < 0.001, **p (or ##p) < 0.01, *p (or #p) < 0.05. **c**, Quantification of the average maximal toe height among groups. **d**, Quantification of the average toe height amplitude among rats with different treatments. One-way ANOVA with Tukey's post hoc test was performed for comparisons among multiple groups (*) and comparisons within groups (#) for the data in the violin plot. ***p (or ###p) < 0.001, **p (or ##p) < 0.01, *p (or #p) < 0.05. **e**, Quantification of the average hip oscillation among rats with different treatments. One-way ANOVA with Tukey's post hoc test was performed for comparisons among multiple groups (*) and comparisons within groups (#) for the data in the violin plot. ***p (or ###p) < 0.001, **p (or ##p) < 0.01, *p (or #p) < 0.05. **f**, Quantification of the average knee angle oscillation among rats with different treatments. One-way ANOVA with Tukey's post hoc test was performed for comparisons among multiple groups (*) and for comparisons within groups (#) for the data shown in the violin plot. ***p (or ###p) < 0.001, **p (or ##p) < 0.01, *p (or #p) < 0.05. **g**, Quantification of the average ankle angle oscillation among rats with different treatments. One-way ANOVA with Tukey's post hoc test was performed for comparisons among multiple groups (*) and for comparisons within groups (#) for the data in the violin plot. ***p (or ###p) < 0.001, **p (or ##p) < 0.01, *p (or #p) < 0.05. **h-i**, Poincaré statistical analysis of the EMG signal amplitude rhythm of TA and GS muscles in the DOPA Nano and GABA Nano groups. One-way ANOVA with

Tukey's post hoc test was performed for comparisons among multiple groups (*) and for comparisons within groups (#) for the data shown in the violin plot. ***p (or ###p) < 0.001, **p (or ##p) < 0.01, *p (or #p) < 0.05. The complete stride cycle of each rat was recorded three times. n = 12 animals for intact group, n = 5 for PBS group, n = 6 for DOPA Nano group and ROS Nano group, n = 7 for GABA Nano group. The violin plot center indicates the median in all planes. Violin range covers 97.5th and 2.5th percentiles; extending whiskers show data distribution and probability density. Violin areas remain constant. Boxplot centerlines signify medians; boxes show first and third quartiles (Q1, Q3); whiskers extend from Q1 - 1.5xIQR to Q3 + 1.5xIQR; outliers lie outside whiskers. ANOVA for hip angle oscillation: Total: F = 19.098377, p = 5.200688*10⁻⁰⁷, GABA-DOPA, p = 2.939199*10⁻⁰⁴, PBS-DOPA, p = 1.637802*10⁻⁰², ROS-GABA, p = 7.304814*10⁻⁰⁶, PBS-GABA, p = 6.557397*10⁻⁰⁸ intact-GABA, p = 8.846887*10⁻⁰⁴. ANOVA for knee angle oscillation Total: F = 8.73049, p = 0.000077, ROS-GABA, p = 0.034070, PBS-GABA p = 0.009822 intact-ROS p = 0.001111 intact-PBS p = 0.000313, ANOVA for ankle angle oscillation Total: F = 19.336293 p = 4.550813*10⁻⁰⁸, GABA-DOPA p = 4.891140*10⁻⁰³ ROS-DOPA P = 2.718774*10⁻⁰², PBS-DOPA p = 1.332916*10⁻⁰³, ROS-GABA p = 1.476894*10⁻⁰⁶, PBS-GABA p = 6.437209*10⁻⁰⁸, intact-GABA p = 1.882720*10⁻⁰⁵, intact-PBS P = 6.527743*10⁻⁰³, ANOVA for Max Height of Crest Total: F = 38.22068, p = 1.439885*10⁻¹¹, intact-PBS p = 2.925660*10⁻¹², intact-ROS p = 1.030447*10⁻⁰⁷, intact-DOPA p = 1.880252*10⁻⁰⁶, intact-GABA p = 1.456296*10⁻⁰⁷, PBS-ROS p = 8.492501*10⁻⁰³, PBS-DOPA p = 9.491884*10⁻⁰³, PBS-GABA P = 2.243848*10⁻⁰³ ANOVA for maximal toe height Total: F = 3.735206 p = 0.013587. ANOVA for Toe Amplitude Total: F = 9.266889 p = 0.000048, intact-PBS p = 0.014311, intact-ROS p = 0.000182, intact-GABA p = 0.000631. ANOVA for crest high amplitude Total: F = 0.632153, p = 0.643303.



Extended Data Fig. 6 | C-Fos expression in T8 and L2 spinal cord sections with different treatments. **a**, Representative images of transverse sections of the T8 spinal cords of injured rats after 9 weeks of treatment with PBS, ROS Nano, DOPA Nano or GABA Nano, stained with c-Fos and NeuN. Scale bar, 500 μ m.

b, Representative images of transverse sections of the L2 spinal cords of injured rats after 9 weeks of treatment with PBS, ROS Nano, DOPA Nano or GABA Nano, stained with c-Fos and NeuN. Scale bar, 500 μ m. T8 represents the 7th thoracic vertebral level, and L2 represents the second Lumbala's vertebral level.

Reporting Summary

Nature Portfolio wishes to improve the reproducibility of the work that we publish. This form provides structure for consistency and transparency in reporting. For further information on Nature Portfolio policies, see our [Editorial Policies](#) and the [Editorial Policy Checklist](#).

Statistics

For all statistical analyses, confirm that the following items are present in the figure legend, table legend, main text, or Methods section.

n/a Confirmed

- The exact sample size (n) for each experimental group/condition, given as a discrete number and unit of measurement
- A statement on whether measurements were taken from distinct samples or whether the same sample was measured repeatedly
- The statistical test(s) used AND whether they are one- or two-sided
Only common tests should be described solely by name; describe more complex techniques in the Methods section.
- A description of all covariates tested
- A description of any assumptions or corrections, such as tests of normality and adjustment for multiple comparisons
- A full description of the statistical parameters including central tendency (e.g. means) or other basic estimates (e.g. regression coefficient) AND variation (e.g. standard deviation) or associated estimates of uncertainty (e.g. confidence intervals)
- For null hypothesis testing, the test statistic (e.g. F , t , r) with confidence intervals, effect sizes, degrees of freedom and P value noted
Give P values as exact values whenever suitable.
- For Bayesian analysis, information on the choice of priors and Markov chain Monte Carlo settings
- For hierarchical and complex designs, identification of the appropriate level for tests and full reporting of outcomes
- Estimates of effect sizes (e.g. Cohen's d , Pearson's r), indicating how they were calculated

Our web collection on [statistics for biologists](#) contains articles on many of the points above.

Software and code

Policy information about [availability of computer code](#)

Data collection

TEM: Tecnai Spirit electron microscope at 120 KV (Thermo, Czech Republic)
 DLS: Litesizer 500 (Anton Paar, Austria)
 NMR: Avance III 500 M (Bruker, Germany)
 GPC: Gel permeation chromatography (GPC)
 inverted fluorescence microscopy (Olympus IX53, Japan)
 confocal laser scanning microscopy (A1Ti, Nikon, Japan)
 virtual digital slice scanning system (VS120, Olympus, Japan)
 in vivo fluorescence imaging system (CRI Corporation, America, MK50101-EX)
 MotoRater (Vicon Motion Systems, UK)
 ChemiDoc Touch Imaging System(Bio-Rad,USA)

Data analysis

For statistics, data were analysed using Graph Prism 8 (8.3.0,GraphPad Software, Inc., USA),Python SciPy(V1.4.1),R language package(3.4.1-x64). For microscopy, images were analysed using Fiji(Windows 64,v1.51,NIH). 3D images were created by Amira software(V.6.01). Electromyography (EMG) data analysis and behavioral assessment were using MATLAB(v2020b).

For manuscripts utilizing custom algorithms or software that are central to the research but not yet described in published literature, software must be made available to editors and reviewers. We strongly encourage code deposition in a community repository (e.g. GitHub). See the Nature Portfolio [guidelines for submitting code & software](#) for further information.

Data

Policy information about [availability of data](#)

All manuscripts must include a [data availability statement](#). This statement should provide the following information, where applicable:

- Accession codes, unique identifiers, or web links for publicly available datasets
- A description of any restrictions on data availability
- For clinical datasets or third party data, please ensure that the statement adheres to our [policy](#)

All data generated or analysed during this study are available in this published article and its supplementary information files or from the corresponding author.

Field-specific reporting

Please select the one below that is the best fit for your research. If you are not sure, read the appropriate sections before making your selection.

Life sciences Behavioural & social sciences Ecological, evolutionary & environmental sciences

For a reference copy of the document with all sections, see nature.com/documents/nr-reporting-summary-flat.pdf

Life sciences study design

All studies must disclose on these points even when the disclosure is negative.

Sample size	No statistical method was used to determine sample size. The sample sizes for experiments on cells and animals were determined from our previously published investigations (Ye, J. et al. Rationally Designed, Self-Assembling, Multifunctional Hydrogel Depot Repairs Severe Spinal Cord Injury. <i>Adv Healthc Mater</i> , e2100242) and was sufficient to yield statistical significance.
Data exclusions	No data was excluded
Replication	All experiments were reasonably designed, including repeated sampling, repeated measurement and repeated experiment, as indicated in the figure legends. All experimental results were reproducible.
Randomization	For cell-based assays, cultured cells were randomly allocated to different experimental groups. For in vivo experiments, rats were randomly assigned to each experimental group before treatment.
Blinding	For in vivo studies, when possible, experimenters were blinded to the group allocation. Blinding was performed when conducting quantitative analysis for immunohistochemical, bioluminescence imaging and quantification, in vivo fluorescence quantification and immunofluorescence. Behavior tests (BBB score) were determined from independent persons who were unaware of the expected therapeutic outcome.

Behavioural & social sciences study design

All studies must disclose on these points even when the disclosure is negative.

Study description	Briefly describe the study type including whether data are quantitative, qualitative, or mixed-methods (e.g. qualitative cross-sectional, quantitative experimental, mixed-methods case study).
Research sample	State the research sample (e.g. Harvard university undergraduates, villagers in rural India) and provide relevant demographic information (e.g. age, sex) and indicate whether the sample is representative. Provide a rationale for the study sample chosen. For studies involving existing datasets, please describe the dataset and source.
Sampling strategy	Describe the sampling procedure (e.g. random, snowball, stratified, convenience). Describe the statistical methods that were used to predetermine sample size OR if no sample-size calculation was performed, describe how sample sizes were chosen and provide a rationale for why these sample sizes are sufficient. For qualitative data, please indicate whether data saturation was considered, and what criteria were used to decide that no further sampling was needed.
Data collection	Provide details about the data collection procedure, including the instruments or devices used to record the data (e.g. pen and paper, computer, eye tracker, video or audio equipment) whether anyone was present besides the participant(s) and the researcher, and whether the researcher was blind to experimental condition and/or the study hypothesis during data collection.
Timing	Indicate the start and stop dates of data collection. If there is a gap between collection periods, state the dates for each sample cohort.
Data exclusions	If no data were excluded from the analyses, state so OR if data were excluded, provide the exact number of exclusions and the rationale behind them, indicating whether exclusion criteria were pre-established.

Non-participation

State how many participants dropped out/declined participation and the reason(s) given OR provide response rate OR state that no participants dropped out/declined participation.

Randomization

If participants were not allocated into experimental groups, state so OR describe how participants were allocated to groups, and if allocation was not random, describe how covariates were controlled.

Ecological, evolutionary & environmental sciences study design

All studies must disclose on these points even when the disclosure is negative.

Study description

Briefly describe the study. For quantitative data include treatment factors and interactions, design structure (e.g. factorial, nested, hierarchical), nature and number of experimental units and replicates.

Research sample

*Describe the research sample (e.g. a group of tagged *Passer domesticus*, all *Stenocereus thurberi* within Organ Pipe Cactus National Monument), and provide a rationale for the sample choice. When relevant, describe the organism taxa, source, sex, age range and any manipulations. State what population the sample is meant to represent when applicable. For studies involving existing datasets, describe the data and its source.*

Sampling strategy

Note the sampling procedure. Describe the statistical methods that were used to predetermine sample size OR if no sample-size calculation was performed, describe how sample sizes were chosen and provide a rationale for why these sample sizes are sufficient.

Data collection

Describe the data collection procedure, including who recorded the data and how.

Timing and spatial scale

Indicate the start and stop dates of data collection, noting the frequency and periodicity of sampling and providing a rationale for these choices. If there is a gap between collection periods, state the dates for each sample cohort. Specify the spatial scale from which the data are taken

Data exclusions

If no data were excluded from the analyses, state so OR if data were excluded, describe the exclusions and the rationale behind them, indicating whether exclusion criteria were pre-established.

Reproducibility

Describe the measures taken to verify the reproducibility of experimental findings. For each experiment, note whether any attempts to repeat the experiment failed OR state that all attempts to repeat the experiment were successful.

Randomization

Describe how samples/organisms/participants were allocated into groups. If allocation was not random, describe how covariates were controlled. If this is not relevant to your study, explain why.

Blinding

Describe the extent of blinding used during data acquisition and analysis. If blinding was not possible, describe why OR explain why blinding was not relevant to your study.

Did the study involve field work? Yes No

Field work, collection and transport

Field conditions

Describe the study conditions for field work, providing relevant parameters (e.g. temperature, rainfall).

Location

State the location of the sampling or experiment, providing relevant parameters (e.g. latitude and longitude, elevation, water depth).

Access & import/export

Describe the efforts you have made to access habitats and to collect and import/export your samples in a responsible manner and in compliance with local, national and international laws, noting any permits that were obtained (give the name of the issuing authority, the date of issue, and any identifying information).

Disturbance

Describe any disturbance caused by the study and how it was minimized.

Reporting for specific materials, systems and methods

We require information from authors about some types of materials, experimental systems and methods used in many studies. Here, indicate whether each material, system or method listed is relevant to your study. If you are not sure if a list item applies to your research, read the appropriate section before selecting a response.

Materials & experimental systems

n/a	Involved in the study
<input type="checkbox"/>	<input checked="" type="checkbox"/> Antibodies
<input type="checkbox"/>	<input checked="" type="checkbox"/> Eukaryotic cell lines
<input checked="" type="checkbox"/>	<input type="checkbox"/> Palaeontology and archaeology
<input type="checkbox"/>	<input checked="" type="checkbox"/> Animals and other organisms
<input checked="" type="checkbox"/>	<input type="checkbox"/> Human research participants
<input checked="" type="checkbox"/>	<input type="checkbox"/> Clinical data
<input checked="" type="checkbox"/>	<input type="checkbox"/> Dual use research of concern

Methods

n/a	Involved in the study
<input checked="" type="checkbox"/>	<input type="checkbox"/> ChIP-seq
<input checked="" type="checkbox"/>	<input type="checkbox"/> Flow cytometry
<input checked="" type="checkbox"/>	<input type="checkbox"/> MRI-based neuroimaging

Antibodies

Antibodies used

Rabbit polyclonal anti-NF ; Abcam Cat# ab134436; dilution 1:500
 Chicken polyclonal anti-GFAP ; Abcam Cat# ab8135; dilution 1:500
 Goat polyclonal anti-5-HT; Invitrogen Cat# pa1-36157; dilution 1:500
 Rabbit recombinant multiclonal anti-iNOS; Abcam Cat# ab283655; dilution 1:200
 Goat polyclonal anti-IBA1; Abcam Cat# ab5076; dilution 1:500
 Rabbit monoclonal anti-NeuN; Abcam Cat# ab177487; dilution 1:500
 Goat polyclonal anti-chicken IgY (H+L); Abcam Cat#ab150172; dilution 1:500
 Rabbit polyclonal anti-TGF- β ;Abclonal Cat# A15103; dilution 1:1000
 Rabbit polyclonal anti-Bcl-2;Abclonal Cat# A0208; dilution 1:1000
 Rabbit polyclonal anti-Bax;Abclonal Cat# A0207; dilution 1:1000
 Rabbit polyclonal anti-cFOS; SYSY Cat# 226 004; dilution 1:200
 Donkey Anti-Chicken IgY H&L (FITC); Abcam Cat# ab63507; dilution 1:500
 Rabbit polyclonal anti-CCL-3 (MIP-1 α);Abclonal Cat# A7568; dilution 1:100
 Rabbit polyclonal anti-GRO; Affinity AF5403; dilution 1:100
 Rabbit polyclonal anti-MCP-1;Thermo Fisher Cat#PA5-115555; dilution 1:200
 Donkey anti-rabbit IgG (H+L) highly cross-adsorbed secondary antibody conjugated with Alexa Fluor 555; Abcam Cat# ab150062; dilution 1:500
 Donkey Anti-Mouse IgG H&L (Alexa Fluor® 488); Abcam Cat# ab150105; dilution 1:500
 Rabbit polyclonal Secondary Antibody to Goat IgG - H&L (Alexa Fluor® 555); Abcam Cat# ab150142; dilution 1:500
 Rabbit polyclonal Secondary Antibody to Goat IgG - H&L (Alexa Fluor® 647); Abcam Cat# ab150147; dilution 1:500
 Donkey anti-rabbit secondary antibodies conjugated with HRP;Abcam Cat# ab205722; dilution 1:10000
 Mouse monoclonal anti-DOPA antibody (anti-HNF-3 β);Santa Cruz Cat#sc-374376; dilution 1:200
 Rabbit monoclonal anti-GABA antibody; Abcam Cat#ab216465 dilution 1:200

Validation

Primary and secondary antibodies are widely used and were characterized by the manufacturer and by controls (including omission of primary or secondary antibodies). Where possible, antibodies are validated as described in:
 Chen, B. et al. Reactivation of Dormant Relay Pathways in Injured Spinal Cord by KCC2 Manipulations. Cell 174, 521-535 e513,
 Gunaseelan S. et al. Pharmacological perturbation of CXCL1 signaling alleviates neuropathogenesis in a model of HEVAT1 infection.Nature communications (2022) 13: 890.
 Ye, J. et al. Rationally Designed, Self-Assembling, Multifunctional Hydrogel Depot Repairs Severe Spinal Cord Injury. Adv Health Mater, Advanced Healthcare Materials(2021)e2100242, doi:10.1002/adhm.202100242 .

Eukaryotic cell lines

Policy information about [cell lines](#)

Cell line source(s)	PC12 cells were from Nanjing cobioer bioscience.co,ltd
Authentication	PC12 cells were authenticated by genomic sequencing.
Mycoplasma contamination	All cell lines used in this study were tested negative for mycoplasma contamination.
Commonly misidentified lines (See ICLAC register)	No commonly misidentified cell lines were used

Palaeontology and Archaeology

Specimen provenance	Provide provenance information for specimens and describe permits that were obtained for the work (including the name of the issuing authority, the date of issue, and any identifying information). Permits should encompass collection and, where applicable, export.
Specimen deposition	Indicate where the specimens have been deposited to permit free access by other researchers.
Dating methods	If new dates are provided, describe how they were obtained (e.g. collection, storage, sample pretreatment and measurement), where they were obtained (i.e. lab name), the calibration program and the protocol for quality assurance OR state that no new dates are

provided.

Tick this box to confirm that the raw and calibrated dates are available in the paper or in Supplementary Information.

Ethics oversight

Identify the organization(s) that approved or provided guidance on the study protocol, OR state that no ethical approval or guidance was required and explain why not.

Note that full information on the approval of the study protocol must also be provided in the manuscript.

Animals and other organisms

Policy information about [studies involving animals; ARRIVE guidelines](#) recommended for reporting animal research

Laboratory animals

Sprague–Dawley rats (200–250 g, about 8 weeks old, female) were purchased from the Experimental Animal Center of the Zhejiang Academy of Medical Science, Hangzhou, China. All animals were housed in a specific pathogen-free environment at ambient temperature (24 ± 2 °C), air humidity 40–70% and 12 h dark/12 h light cycle.

Wild animals

No wild animals were used in this study.

Field-collected samples

This study did not involve any sample collected from the field.

Ethics oversight

All animal protocols were approved by the Institutional Animal Care and used following the provisions of Zhejiang University Animal Experimentation Committee (ZJU20201010).

Note that full information on the approval of the study protocol must also be provided in the manuscript.

Human research participants

Policy information about [studies involving human research participants](#)

Population characteristics

Describe the covariate-relevant population characteristics of the human research participants (e.g. age, gender, genotypic information, past and current diagnosis and treatment categories). If you filled out the behavioural & social sciences study design questions and have nothing to add here, write "See above."

Recruitment

Describe how participants were recruited. Outline any potential self-selection bias or other biases that may be present and how these are likely to impact results.

Ethics oversight

Identify the organization(s) that approved the study protocol.

Note that full information on the approval of the study protocol must also be provided in the manuscript.

Clinical data

Policy information about [clinical studies](#)

All manuscripts should comply with the ICMJE [guidelines for publication of clinical research](#) and a completed [CONSORT checklist](#) must be included with all submissions.

Clinical trial registration

Provide the trial registration number from ClinicalTrials.gov or an equivalent agency.

Study protocol

Note where the full trial protocol can be accessed OR if not available, explain why.

Data collection

Describe the settings and locales of data collection, noting the time periods of recruitment and data collection.

Outcomes

Describe how you pre-defined primary and secondary outcome measures and how you assessed these measures.

Dual use research of concern

Policy information about [dual use research of concern](#)

Hazards

Could the accidental, deliberate or reckless misuse of agents or technologies generated in the work, or the application of information presented in the manuscript, pose a threat to:

No Yes

- | | |
|--------------------------|---|
| <input type="checkbox"/> | <input type="checkbox"/> Public health |
| <input type="checkbox"/> | <input type="checkbox"/> National security |
| <input type="checkbox"/> | <input type="checkbox"/> Crops and/or livestock |
| <input type="checkbox"/> | <input type="checkbox"/> Ecosystems |
| <input type="checkbox"/> | <input type="checkbox"/> Any other significant area |

Experiments of concern

Does the work involve any of these experiments of concern:

- | | |
|--------------------------|---|
| No | Yes |
| <input type="checkbox"/> | Demonstrate how to render a vaccine ineffective |
| <input type="checkbox"/> | Confer resistance to therapeutically useful antibiotics or antiviral agents |
| <input type="checkbox"/> | Enhance the virulence of a pathogen or render a nonpathogen virulent |
| <input type="checkbox"/> | Increase transmissibility of a pathogen |
| <input type="checkbox"/> | Alter the host range of a pathogen |
| <input type="checkbox"/> | Enable evasion of diagnostic/detection modalities |
| <input type="checkbox"/> | Enable the weaponization of a biological agent or toxin |
| <input type="checkbox"/> | Any other potentially harmful combination of experiments and agents |

Flow Cytometry

Plots

Confirm that:

- The axis labels state the marker and fluorochrome used (e.g. CD4-FITC).
- The axis scales are clearly visible. Include numbers along axes only for bottom left plot of group (a 'group' is an analysis of identical markers).
- All plots are contour plots with outliers or pseudocolor plots.
- A numerical value for number of cells or percentage (with statistics) is provided.

Methodology

Sample preparation

Describe the sample preparation, detailing the biological source of the cells and any tissue processing steps used.

Instrument

Identify the instrument used for data collection, specifying make and model number.

Software

Describe the software used to collect and analyze the flow cytometry data. For custom code that has been deposited into a community repository, provide accession details.

Cell population abundance

Describe the abundance of the relevant cell populations within post-sort fractions, providing details on the purity of the samples and how it was determined.

Gating strategy

Describe the gating strategy used for all relevant experiments, specifying the preliminary FSC/SSC gates of the starting cell population, indicating where boundaries between "positive" and "negative" staining cell populations are defined.

- Tick this box to confirm that a figure exemplifying the gating strategy is provided in the Supplementary Information.

Magnetic resonance imaging

Experimental design

Design type

Indicate task or resting state; event-related or block design.

Design specifications

Specify the number of blocks, trials or experimental units per session and/or subject, and specify the length of each trial or block (if trials are blocked) and interval between trials.

Behavioral performance measures

State number and/or type of variables recorded (e.g. correct button press, response time) and what statistics were used to establish that the subjects were performing the task as expected (e.g. mean, range, and/or standard deviation across subjects).

Acquisition

Imaging type(s)

Specify: functional, structural, diffusion, perfusion.

Field strength

Specify in Tesla

Sequence & imaging parameters

Specify the pulse sequence type (gradient echo, spin echo, etc.), imaging type (EPI, spiral, etc.), field of view, matrix size, slice thickness, orientation and TE/TR/flip angle.

Area of acquisition

State whether a whole brain scan was used OR define the area of acquisition, describing how the region was determined.

Diffusion MRI

 Used Not used

Preprocessing

Preprocessing software

Provide detail on software version and revision number and on specific parameters (model/functions, brain extraction, segmentation, smoothing kernel size, etc.).

Normalization

If data were normalized/standardized, describe the approach(es): specify linear or non-linear and define image types used for transformation OR indicate that data were not normalized and explain rationale for lack of normalization.

Normalization template

Describe the template used for normalization/transformation, specifying subject space or group standardized space (e.g. original Talairach, MNI305, ICBM152) OR indicate that the data were not normalized.

Noise and artifact removal

Describe your procedure(s) for artifact and structured noise removal, specifying motion parameters, tissue signals and physiological signals (heart rate, respiration).

Volume censoring

Define your software and/or method and criteria for volume censoring, and state the extent of such censoring.

Statistical modeling & inference

Model type and settings

Specify type (mass univariate, multivariate, RSA, predictive, etc.) and describe essential details of the model at the first and second levels (e.g. fixed, random or mixed effects; drift or auto-correlation).

Effect(s) tested

Define precise effect in terms of the task or stimulus conditions instead of psychological concepts and indicate whether ANOVA or factorial designs were used.

Specify type of analysis: Whole brain ROI-based Both

Statistic type for inference (See [Eklund et al. 2016](#))

Specify voxel-wise or cluster-wise and report all relevant parameters for cluster-wise methods.

Correction

Describe the type of correction and how it is obtained for multiple comparisons (e.g. FWE, FDR, permutation or Monte Carlo).

Models & analysis

n/a

Involved in the study

- Functional and/or effective connectivity
- Graph analysis
- Multivariate modeling or predictive analysis

Functional and/or effective connectivity

Report the measures of dependence used and the model details (e.g. Pearson correlation, partial correlation, mutual information).

Graph analysis

Report the dependent variable and connectivity measure, specifying weighted graph or binarized graph, subject- or group-level, and the global and/or node summaries used (e.g. clustering coefficient, efficiency, etc.).

Multivariate modeling and predictive analysis

Specify independent variables, features extraction and dimension reduction, model, training and evaluation metrics.